Simulation of Ca^{2+} Movements within the Sarcomere of Fast-Twitch Mouse Fibers Stimulated by Action Potentials

Stephen M. Baylor and Stephen Hollingworth

Department of Physiology, University of Pennsylvania School of Medicine, Philadelphia, PA 19104

Ca^{2+} release from the sarcoplasmic reticulum (SR) of skeletal muscle takes place at the triadic junctions; following release, Ca^{2+} spreads within the sarcomere by diffusion. Here, we report multicompartment simulations of changes in sarcomeric Ca^{2+} evoked by action potentials (APs) in fast-twitch fibers of adult mice. The simulations include Ca^{2+} complexation reactions with ATP, troponin, parvalbumin, and the SR Ca^{2+} pump, as well as Ca^{2+} transport by the pump. Results are compared with spatially averaged Ca^{2+} transients measured in mouse fibers with furaptra, a low-affinity, rapidly responding Ca^{2+} indicator. The furaptra Δf_{CaD} signal (change in the fraction of the indicator in the Ca^{2+}-bound form) evoked by one AP is well simulated under the assumption that SR Ca^{2+} release has a peak of 200–225 μM/ms and a FDHM of ~1.6 ms (16°C). Δf_{CaD} elicited by a five-shock, 67-Hz train of APs is well simulated under the assumption that in response to APs 2–5, Ca^{2+} release decreases progressively from 0.25 to 0.15 times that elicited by the first AP, a reduction likely due to Ca^{2+} inactivation of Ca^{2+} release. Recovery from inactivation was studied with a two-AP protocol; the amplitude of the second release recovered to >0.9 times that of the first with a rate constant of 7 s^{-1}. An obvious feature of Δf_{CaD} during a five-shock train is a progressive decline in the rate of decay from the individual peaks of Δf_{CaD}. According to the simulations, this decline is due to a reduction in available Ca^{2+} binding sites on troponin and parvalbumin. The effects of sarcomere length, the location of the triadic junctions, resting $[Ca^{2+}]$, the parvalbumin concentration, and possible uptake of Ca^{2+} by mitochondria were also investigated. Overall, the simulations indicate that this reaction-diffusion model, which was originally developed for Ca^{2+} sparks in frog fibers, works well when adapted to mouse fast-twitch fibers stimulated by APs.

The Journal of General Physiology

INTRODUCTION

During normal excitation–contraction (EC) coupling of vertebrate twitch fibers, an action potential (AP) elicits a large and rapid release of Ca^{2+} from the SR. As a result, myoplasmic free $[Ca^{2+}]$ rises quickly to a high level near the triadic junctions, the location of the SR Ca^{2+} release channels. Ca^{2+} then spreads by diffusion throughout the sarcomere while binding to sites on myoplasmic Ca^{2+} buffers, including ATP, troponin, parvalbumin, and the SR Ca^{2+} pump. On a longer time scale, the released Ca^{2+} is resequestered within the SR by ATP-dependent transport by the SR Ca^{2+} pump.

Kinetic models have been used to describe some, but not all, of these events in the setting of a functioning muscle cell. The earliest models started with an assumed (Robertson et al., 1981) or measured (Baylor et al., 1983) waveform of the change in (spatially averaged) free $[Ca^{2+}]$ ($\Delta[Ca^{2+}]$) or an assumed waveform of SR Ca^{2+} release (Gillis et al., 1982); the diffusion of Ca^{2+} and its mobile buffers was ignored. Also ignored were effects due to binding of Ca^{2+} by the SR Ca^{2+} pump. The model of Cannell and Allen (1984) was the first to consider the diffusive aspects of the problem. The myoplasm of a half sarcomere of a myofibril of a frog twitch fiber was subdivided into a large number of compartments of equal volume; radial symmetry was assumed. AP-evoked activity was initiated by SR Ca^{2+} release into one compartment, and changes in Ca^{2+} binding and diffusion were calculated for each compartment by integration of a large set of simultaneous first-order differential equations; transport, but not binding, of Ca^{2+} by the SR Ca^{2+} pump was included. To link the model to experiments, the spatially averaged luminescence change from aequorin was simulated. An acceptable level of agreement was observed between the simulated and measured aequorin signals, which supported the basic concepts of the model. An important conclusion was that large gradients in $[Ca^{2+}]$ exist within the sarcomere during, and for a few tens of milliseconds after, SR Ca^{2+} release (20°C).

A similar multicompartment model was developed by Baylor and Hollingworth (1998) to simulate AP-evoked Ca^{2+} movements in frog twitch fibers (16°C). This model incorporated more up-to-date information about the time course of SR Ca^{2+} release and included ATP as a myoplasmic Ca^{2+} buffer. The experimental comparison for these simulations was with $\Delta[Ca^{2+}]$ estimated with furaptra (Raju et al., 1989), a rapidly responding fluorescent Ca^{2+} indicator with 1:1 stoichiometry (Ca^{2+}:indicator). These simulations confirmed the existence

Correspondence to S.M. Baylor: baylor@mail.med.upenn.edu

Abbreviations used in this paper: AP, action potential; EC, excitation–contraction; EDL, extensor digitorum longus; FDHM, full duration at half maximum; RyR, ryanodine receptor.

of large gradients in $\Delta[Ca^{2+}]$ within the sarcomere during and shortly after SR Ca^{2+} release. A novel finding was that Ca^{2+} binding by ATP and the diffusion of CaATP have a strong influence on the amplitude and time course with which Ca^{2+} binds to troponin at different locations along the thin filament.

Similar multicompartment simulations have not yet been reported for mammalian fibers. Mammalian Ca^{2+} measurements have been the focus of much recent work, including investigations into alterations in Ca^{2+} homeostasis by drugs and diseases (e.g., Dirksen and Avila, 2004; Woods et al., 2004; Capote et al., 2005; Yeung et al., 2005; Brown et al., 2007; Pouvreau et al., 2007). Thus, it is important to establish valid modeling methods for interpretation of Ca^{2+} measurements in mammalian muscle. Although it is expected that many of the conclusions from the amphibian studies may apply to mammalian fibers, there are structural, biochemical, and physiological differences between mammalian and amphibian fibers that will influence the results and, possibly, the interpretations. For example, in mammals, the triadic junctions are offset ~0.5 μm from the z line (Smith, 1966; Eisenberg, 1983; Brown et al., 1998), whereas, in amphibians, the junctions are located at the z line. The functional properties of the dihydropyridine receptors, the voltage sensors of EC coupling, are also different, as indicated by differences in the amount and voltage dependence of muscle charge movement (e.g., Hollingworth and Marshall, 1981). Differences are also found in the organization of the ryanodine receptors (RyRs), the Ca^{2+} release channels of the SR, at the triadic junction. In fibers from mammalian limb muscles (which are used in the experiments in our laboratory), the RyRs are found in junctional arrays only, whereas, in amphibian fibers, both junctional and parajunctional arrays are present (Felder and Franzini-Armstrong, 2002). Moreover, adult mammalian limb fibers have only the RyR1 isoform (Conti et al., 1996; Flucher et al., 1999), whereas amphibian fibers have a nearly equal mixture of the RyR1 and RyR3 isoforms (sometimes referred to as RyRα and RyRβ) (Olivares et al., 1991; Lai et al., 1992; Murayama and Ogawa, 1992; O'Brien et al., 1993). Finally, the time course of $\Delta[Ca^{2+}]$ evoked by an AP is significantly different in mammalian and amphibian fibers. At 16°C, the FDHM (full duration at half maximum) of $\Delta[Ca^{2+}]$ in mouse fast-twitch fibers is ~5 ms, whereas, in frog twitch fibers of similar diameter, it is 8–9 ms (Hollingworth et al., 1996).

In this article, we report multicompartment simulations of sarcomeric Ca^{2+} movements evoked by APs in mouse fast-twitch fibers. The results are compared with spatially averaged Ca^{2+} transients measured in these fibers with furaptra and with simulations based on a single-compartment model. This article also examines how sarcomere length, the location of the triadic junctions, the resting level of $[Ca^{2+}]$ ($[Ca^{2+}]_R$), the presence of parvalbumin, and the possible uptake of Ca^{2+} by mitochondria are expected to affect the results.

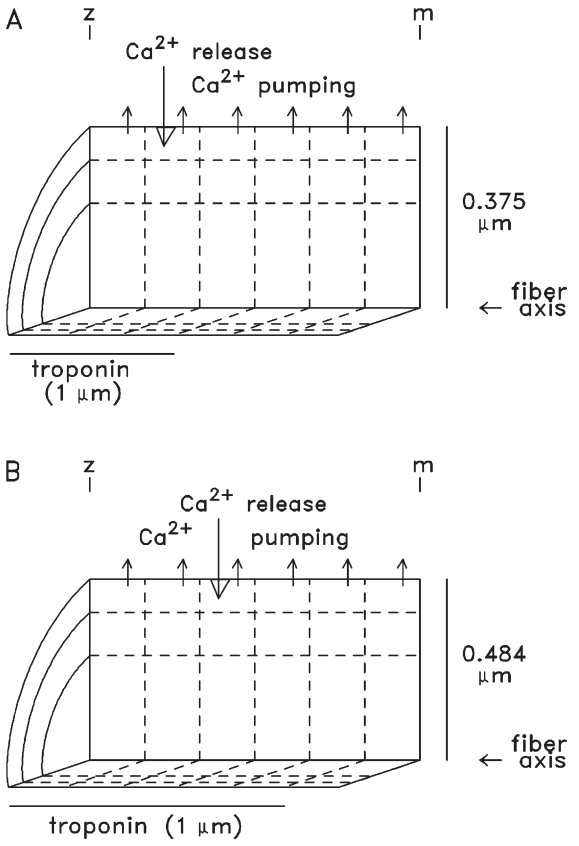

Figure 1. Cut-away view of a half sarcomere of one myofibril showing the arrangement of the 18 equal-volume compartments (six longitudinal × three radial) in the simulations at a sarcomere length of 4 μm (A) and 2.4 μm (B). SR Ca^{2+} release enters the myoplasm near the middle of the thin filament in the outer compartment row (large downward arrow); Ca^{2+} pump activity occurs within all compartments in the outer row (small upward arrows). In both arrangements, troponin is restricted to the compartments located within 1 μm of the z-line (the region containing thin filaments, average length ~1 μm). Because the buffer concentrations in Table I are averages over the entire myoplasmic volume, the actual compartment concentration of troponin is 2.0 (A) or 1.2 (B) times the value listed in Table I, and the actual compartment concentration of Ca^{2+} pump molecules is three times (both A and B) the value listed in Table I. In both parts, the vertical and horizontal calibrations are different and not to scale.

A preliminary version of the results has appeared in abstract form (Baylor, S.M., and S. Hollingworth. 2007. *Biophys. J.* 92:311a).

MATERIALS AND METHODS

Simulations

A multicompartment model was used to simulate myoplasmic Ca^{2+} binding and diffusion as well as SR Ca^{2+} transport in mouse EDL (extensor digitorum longus) fibers activated by APs (16°C). Simulations were performed for a half sarcomere of a myofibril, which is divided into 18 equal volume units (six longitudinal by three radial; Fig. 1) at two sarcomere lengths, 4.0 (Fig. 1 A) and

TABLE I

Concentrations of Myoplasmic Constituents in Mouse EDL Fibers

1	2	3
Constituent	Concentration (μM)	Concentration of binding sites (μM)
resting [Ca^{2+}]	0.050	–
resting [Mg^{2+}]	1,000	–
troponin	120	240 (Ca^{2+} regulatory sites)
SR Ca^{2+} pump	120	240 (Ca^{2+} transport sites)
parvalbumin	750	1,500 (Ca^{2+}/Mg^{2+} sites)
ATP	8,000	8,000 (Ca^{2+}/Mg^{2+} sites)
furaptra	100	100 (Ca^{2+}/Mg^{2+} sites)
protein	500	500 (furaptra sites)

Concentrations are spatially averaged and referred to the myoplasmic water volume (Baylor et al., 1983); except for free [Ca^{2+}] and free [Mg^{2+}], total concentrations are given. Except for furaptra and protein, the values assumed here for EDL fibers are the same as those given by Hollingworth et al. (2006) for frog twitch fibers. The furaptra and protein concentrations apply to Fig. 2 E and Table II (E). pH is assumed to be 7 and constant.

2.4 μm (Fig. 1 B). The myofibrillar radii were 0.375 and 0.484 μm, respectively, and the computational water volume was 0.884 fL in both cases. The calculations were performed with MLAB (Civilized Software). An 18-compartment model appears to be sufficient for the simulations of this article; in a study of Ca^{2+} binding and diffusion evoked by an AP in frog fibers, simulations of the fluo-3 Ca^{2+} signal performed with an 18- and a 100-compartment model yielded similar results (Hollingworth et al., 2000).

Ca^{2+} Binding and Diffusion. Each compartment is assumed to contain furaptra and an appropriate concentration of the major myoplasmic Ca^{2+} buffers—ATP, troponin, parvalbumin, and the SR Ca^{2+} pump (Table I and Fig. 1, legend). A set of differential equations is specified for each compartment that describes (a) the binding of Ca^{2+} (and, in some cases, Mg^{2+} and H^+) to these buffers according to the reaction schemes in Fig. 2 and the reaction rate constants in Table II, and (b) the diffusion of free Ca^{2+} and the mobile Ca^{2+} buffers across compartment boundaries according to the diffusion coefficients in Table III, B. The simulations assume that $[Ca^{2+}]_R$ is 50 nM, that free [Mg^{2+}] is 1 mM (and constant), and that pH is 7 (and constant). These features are the same as those in spark Model 3 of Hollingworth et al. (2006), apart from small adjustments to the reaction rate constants and diffusion constants due to the temperature difference of the experiments (16 vs. 18°C; see legend to Table II) and the use of furaptra rather than fluo-3 as the Ca^{2+} indicator.

Ca^{2+} Pumping. Because the SR membrane surrounds the periphery of a sarcomere, Ca^{2+} pump activity was assigned to the outer row of compartments (small upward arrows in Fig. 1). The reaction scheme of the Ca^{2+} pump is the same as in spark Model 3; the ion binding steps (first eight reactions in Table II, D) are those given by Peinelt and Apell (2002). With this scheme and the resting values of [Ca^{2+}], [Mg^{2+}], and pH in Table I, only 0.6% of the transport sites are immediately available to bind Ca^{2+} when [Ca^{2+}] suddenly rises (see legend of Fig. 2). This feature, which introduces a delay in Ca^{2+} binding and transport by the Ca^{2+} pump following SR Ca^{2+} release, increases the efficiency of excitation–contraction coupling in the sense that less Ca^{2+} release is required to achieve a given level of saturation of troponin with Ca^{2+} (Hollingworth et al., 2006).

Ca^{2+} Release. In mammalian fibers, the triadic junctions are located at the periphery of a myofibril in a narrow region that is offset ~0.5 μm from the z-line, both in slack and stretched fibers (Brown et al., 1998). This Ca^{2+} release location is consistent with the experiments of Gomez et al. (2006) on mouse fast-twitch fibers from flexor digitorum brevis muscle stimulated by APs, in which Ca^{2+} release domains offset ~0.5 μm from the z-line were detected with confocal microscopy. In the simulations, the SR Ca^{2+} release flux is assumed to enter the outer compartment that includes the region 0.5 μm from the z-line; for the simulations at sarcomere lengths 4.0 and 2.4 μm, this is the second and third compartment, respectively (large downward arrows in Fig. 1).

The time course of SR Ca^{2+} release in response to an AP was calculated with an empirical function (compare Baylor and Hollingworth, 1998):

$$\begin{aligned} &Ca^{2+}\ \text{Release}(t) = 0 \text{ if } t < T, \\ &= R \cdot [1 - \exp(-(t-T)/\tau 1)]^L \cdot \exp(-(t-T)/\tau 2) \text{ if } t \geq T. \end{aligned} \quad (1)$$

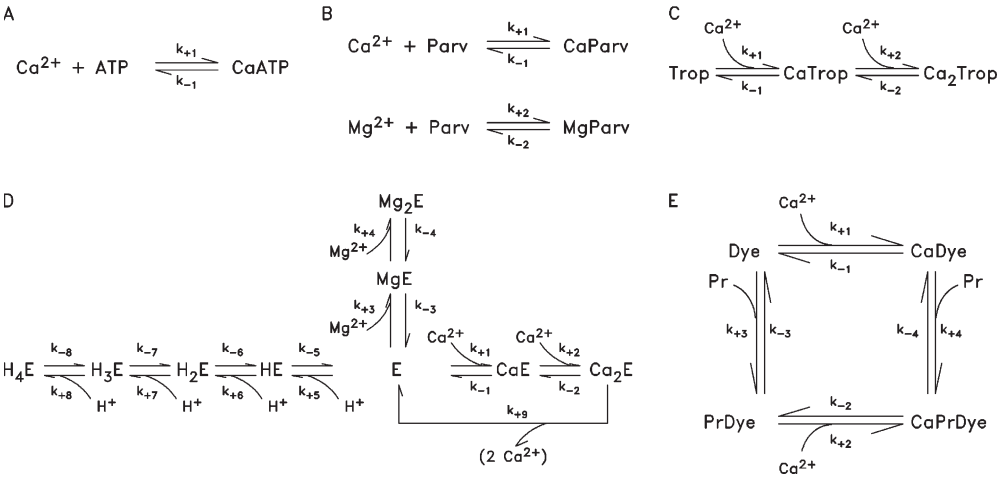

Figure 2. Reaction schemes for ATP (A), parvalbumin (B), troponin (C), the SR Ca^{2+} pump (D), and furaptra (=Dye; E). Table I gives the total reactant concentrations and Table II the reaction rate constants. With the resting values of free [Ca^{2+}], free [Mg^{2+}], and pH in Table I, the fractional amounts of the various reactants at rest are (A) ATP (1.000), CaATP (0.000); (B) Parv (0.062), CaParv (0.258), MgParv (0.680); (C) Trop (0.993), CaTrop (0.006), Ca_2Trop (0.001); (D) E (0.006), CaE (0.006), Ca_2E (0.004), MgE (0.123), Mg_2E (0.123), HE (0.062), H_2E (0.615), H_3E (0.062), H_4E (0.001); (E) Dye (0.451), CaDye (0.000), PrDye (0.548), CaPrDye (0.000). The resting fraction of furaptra in the protein-bound form, 0.548, is approximately consistent with that estimated from furaptra's apparent myoplasmic diffusion coefficient, 0.68×10^{-6} $cm^2 s^{-1}$, measured in frog twitch fibers at 16°C (Konishi et al., 1991). From this diffusion coefficient, Zhao et al. (1996) estimated that the fraction of furaptra in the protein-bound form in resting frog fibers is 0.58.

TABLE II

Rate Constants for the Reactions shown in Fig. 2 (16 °C)

1	2	3	4
Reaction	Forward	Reverse	Ratio
A.			
Ca^{2+} + ATP ⇋ CaATP	*0.1364 × $10^8 M^{-1}s^{-1}$	30,000 s^{-1}	2,200 μM
B.			
Ca^{2+} + Parv ⇋ CaParv	0.417 × $10^8 M^{-1}s^{-1}$	0.5 s^{-1}	0.012 μM
Mg^{2+} + Parv ⇋ MgParv	0.33 × $10^5 M^{-1}s^{-1}$	3 s^{-1}	91.0 μM
C.			
Ca^{2+} + Trop ⇋ CaTrop	1.77 × $10^8 M^{-1}s^{-1}$	1,544 s^{-1}	8.72 μM
Ca^{2+} + CaTrop ⇋ Ca_2Trop	0.885 × $10^8 M^{-1}s^{-1}$	17.1 s^{-1}	0.194 μM
D.			
Ca^{2+} + E ⇋ CaE	1.74 × 10^8 M^{-1} s^{-1}	6.97 s^{-1}	0.04 μM
Ca^{2+} + CaE ⇋ Ca_2E	1.74 × 10^8 M^{-1} s^{-1}	8.71 s^{-1}	0.05 μM
Mg^{2+} + E ⇋ MgE	8.71 × 10^4 M^{-1} s^{-1}	4.36 s^{-1}	50 μM
Mg^{2+} + MgE ⇋ Mg_2E	8.71 × 10^4 M^{-1} s^{-1}	87.1 s^{-1}	1,000 μM
H^+ + E ⇋ HE	instantaneous	instantaneous	(pK=8)
H^+ + HE ⇋ H_2 E	instantaneous	instantaneous	(pK=8)
H^+ + H_2E ⇋ H_3E	instantaneous	instantaneous	(pK=6)
H^+ + H_3E ⇋ H_4E	instantaneous	instantaneous	(pK=5)
Ca_2E ⇋ E + (2 Ca^{2+})	3.48 s^{-1}	0	0
E.			
Ca^{2+} + Dye ⇋ CaDye	2.33 × $10^8 M^{-1}s^{-1}$	11,416 s^{-1}	49 μM
Pr + Dye ⇋ PrDye	0.100 × $10^8 M^{-1}s^{-1}$	3,660 s^{-1}	366 μM
Ca^{2+} + PrDye ⇋ CaPrDye	0.466 × $10^8 M^{-1}s^{-1}$	4,909 s^{-1}	105 μM
Pr + CaDye ⇋ CaPrDye	0.100 × $10^8 M^{-1}s^{-1}$	7,869 s^{-1}	787 μM

Letters A–E correspond to the reactions in panels A–E of Fig. 2, where forward (column 2) and reverse (column 3) rate constants are denoted by k_{+i} and k_{-i} (i = 1, 2, etc.), respectively. Column 4 gives the dissociation constant ($=k_{-i}/k_{+i}$). The rate constants were obtained by scaling those of Hollingworth et al. (2006) at 18°C by the factor 0.871, which corresponds to a Q_{10} of 2. In A, the asterisk in column 2 denotes an apparent rate constant at free [Mg^{2+}] = 1 mM, [K^+] = 0.15 M, pH = 7, and viscosity = 2 centipoise (see Baylor and Hollingworth, 1998). In D, the dissociation constants of the reactions with H^+ are expressed as pKs (shown in parentheses); the parentheses on the righthand side of the last reaction in column 1 denote the two Ca^{2+} ions transported by the pump to the lumen of the SR. In E, "Dye" denotes furaptra and "Pr" denotes protein sites capable of binding furaptra. Steady-state calculations with the scheme in E show that with the protein concentration in Table I, the relation between free [Ca^{2+}] and the fraction of furaptra in the Ca^{2+}-bound form (Δf_{CaD} = ([CaDye]+[CaPrDye])/[Dye_{Total}]) is very accurately described by a 1:1 binding equation with an apparent K_D of 70 μM, the value estimated for frog myoplasm under steady-state conditions (Baylor and Hollingworth, 1998). However, when the peak of Δ[Ca^{2+}] elicited by an AP is calculated from Δf_{CaD} in a single-compartment calibration (Eq. 3), a larger K_D, 96 μM, is required (see Materials and Methods and Baylor and Hollingworth, 1998).

The time-shift parameter T was set to 1.4 ms to simulate the delay from the time of AP generation to the onset of SR Ca^{2+} release. L, τ1, and τ2 were set to 5, 1.3 ms, and 0.5 ms, respectively, so that the FDHM of the release flux would be 1.6 ms, the same as the mean value estimated from the 11 fibers of this study in a single-compartment analysis of their furaptra Ca^{2+} transients (compare last section of Results). The value of R was adjusted to give good agreement between the amplitudes of the simulated and measured furaptra Ca^{2+} transients (next section).

Experimental Procedures

Spatially averaged myoplasmic Ca^{2+} signals evoked by APs were measured with furaptra (also known as mag-fura-2) in intact EDL fibers from 6–14-wk-old mice. Furaptra is a fluorescent indicator whose dissociation constant for Ca^{2+} is relatively large (49 μM in a standard salt solution with 1 mM Mg^{2+}; 16°C) and which responds rapidly to Δ[Ca^{2+}] in muscle fibers (Konishi et al., 1991; Rome et al., 1996). Because furaptra's dissociation constant for Mg^{2+} is large (5.3 mM in a standard salt solution at 16°C), interference in the Ca^{2+} measurements from changes in [Mg^{2+}] are expected to be small. As argued previously (Baylor and Hollingworth, 2003), furaptra appears to supply the most accurate measurements to date of (spatially averaged) Δ[Ca^{2+}] in mammalian muscle fibers stimulated by APs.

Most results from the furaptra EDL experiments were reported previously (Hollingworth et al., 1996; Baylor and Hollingworth, 2003); the results with the two-AP protocol (see Figs. 10 and 11) are new to this study. In each experiment, one fiber within a small, manually dissected bundle of fibers was microinjected with a membrane-impermeant form of furaptra (K_4mag-fura-2; Invitrogen); the average myoplasmic furaptra concentration was ∼0.1 mM. To minimize movement artifacts in the fluorescence records, the fibers were stretched to long-sarcomere length, 3.8 ± 0.2 μm (mean ± SD). $\Delta F/F_R$, the change in indicator fluorescence divided by its resting fluorescence, was recorded from a ∼300-μm length of fiber in response to either one external shock, a five-shock train at 67 Hz, or two shocks separated by a delay of 15 to 400 ms. In most experiments, the fluorescence excitation and emission wavelengths were 410 ± 20 nm and >480 nm, respectively.

Comparisons between the Multicompartment Simulations and the Measurements

The signal that can be most directly compared between the simulations and the measurements is the spatially averaged change in

TABLE III

Values of Other Parameters in the Multicompartment Simulations

A. Structural parameters	(μm)
Length of the thin filament	1.0
Distance from z- to m-line	2.0 and 1.2
Radius of a myofibril	0.375 and 0.484
B. Diffusion coefficients (16 °C)	(10^{-6} cm^2 s^{-1})
Free Ca^{2+}	3
ATP	1.4
Parvalbumin	0.15
Furaptra (protein-free)	1.59

The myofibrillar radii of 0.375 and 0.484 μm are for half-sarcomere lengths of 2.0 and 1.2 μm, respectively. The diffusion coefficients of ATP and furaptra apply to both the Ca^{2+}-free and Ca^{2+}-bound forms; the diffusion coefficient for parvalbumin applies to the Ca^{2+}-bound, Mg^{2+}-bound, and metal-free forms. Troponin, the SR Ca^{2+} pump, and protein-bound furaptra are considered to be nondiffusible.

the fraction of furaptra bound with Ca^{2+} (denoted Δf_{CaD}). The spatially averaged $\Delta F/F_R$ measurements were converted to spatially averaged Δf_{CaD} as described previously (Hollingworth et al., 1996; Baylor and Hollingworth, 2003). With 410-nm excitation, Δf_{CaD} is calculated from $\Delta F/F_R$ with the equation:

$$\Delta f_{CaD} = -1.07\Delta F/F_R. \quad (2)$$

Spatially averaged Δf_{CaD} in the simulations was obtained by averaging the simulated Δf_{CaD} waveforms in the 18 compartments. These waveforms, which include changes in both protein-free and protein-bound indicator (Fig. 2 E and Table II, E), were calculated as $(\Delta[CaDye]+\Delta[CaPrDye])/[Dye_{Total}]$, where $[Dye_{Total}]$ is the total furaptra concentration (usually 100 μM, Table I). Within each compartment, the time courses of the Δ[CaDye] and Δ[CaPrDye] waveforms were always virtually identical; peak Δ[CaDye], however, was always somewhat larger than peak Δ[CaPrDye] (see dissociation constants in Table II, E).

Single-Compartment Estimation of $\Delta[Ca^{2+}]$ from Δf_{CaD}

For single-compartment modeling (compare Figs. 3 and 4 and the last section of Results), Δf_{CaD} was converted to (spatially averaged) $\Delta[Ca^{2+}]$ with the equation:

$$\Delta[Ca^{2+}] = K_D \Delta f_{CaD} / (1 - \Delta f_{CaD}). \quad (3)$$

Eq. 3 is based on the idea of a spatially uniform, kinetically rapid, 1:1 binding reaction between furaptra and Ca^{2+}. K_D, furaptra's apparent dissociation constant for Ca^{2+} in the myoplasm, is assumed to be 96 μM (Hollingworth et al., 1996; Baylor and Hollingworth, 2003). This K_D was selected previously to make the estimated peak of $\Delta[Ca^{2+}]$ evoked by an AP in a frog twitch fiber match that estimated with PDAA (purpurate diacetic acid) (Konishi et al., 1991). PDAA is a rapidly responding absorbance indicator whose fractional binding to myoplasmic constituents of large molecular weight is relatively small (0.2–0.5; Hirota et al., 1989; Konishi and Baylor, 1991) and whose K_D for Ca^{2+} (0.9 mM in a standard salt solution) is sufficiently large that nonlinearities in Ca^{2+} binding near the SR Ca^{2+} release sites is expected to be small (Hirota et al., 1989). In contrast, with furaptra, whose K_D is an order of magnitude smaller, substantial nonlinear responses are expected near the release sites, while nearly linear responses are expected in regions removed from the release sites. It is expected that use of Eq. 3 to estimate $\Delta[Ca^{2+}]$ evoked by APs cannot be accurate at all time points because of the nonlinear Ca^{2+} binding by furaptra near the release sites (Baylor and Hollingworth, 1998; see also Results and legend to Table II).

RESULTS

The uppermost traces in Fig. 3 show Δf_{CaD} of furaptra averaged from four experiments in which an EDL fiber was activated by one AP (panel A) and a five-shock, 67- Hz train of APs (panel B; note difference in time scales). The second row of traces in these panels shows $\Delta[Ca^{2+}]$ calculated from Δf_{CaD} with Eq. 3. Fig. 3 (C and D) shows

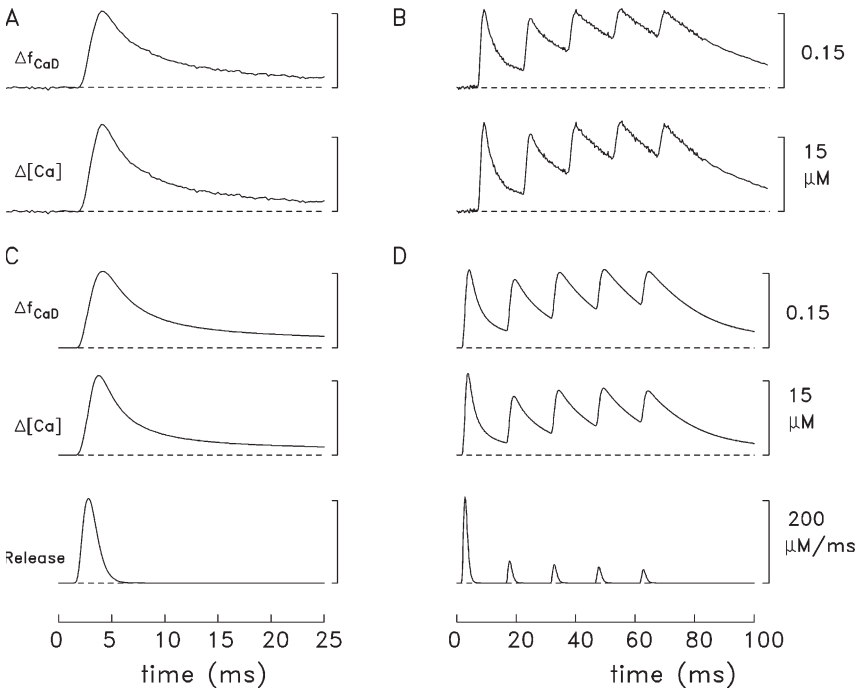

Figure 3. Spatially averaged responses elicited by a single AP (left) and a 67-Hz train of 5 APs (right) initiated at 0 time. (A and B) Experimental Δf_{CaD} and $\Delta[Ca^{2+}]$ responses averaged from four fibers in which Δf_{CaD} was relatively free of movement artifacts; $\Delta[Ca^{2+}]$ was calculated from Δf_{CaD} with Eq. 3 in Materials and Methods. The mean sarcomere length was 3.8 μm (range, 3.7–3.9 μm) and the mean myoplasmic concentration of furaptra was 89 μM (range, 64–113 μM). Fiber identification numbers: 032596.2, 040596.1, 040896.1, and 040996.3. (C and D) Δf_{CaD} and $\Delta[Ca^{2+}]$ responses averaged over the 18 compartments in the multicompartment simulations. The bottom traces show the release fluxes used to drive the simulations. The peaks of the release fluxes are 205 μM/ms in C and 208, 53, 45, 38, and 32 μM/ms in D (APs 1–5, respectively); the FDHM of all release fluxes is 1.6 ms. The values of $\Delta[Ca_{Total}]$ are 349 μM in C and 354, 90, 76, 66, and 55 μM in D.

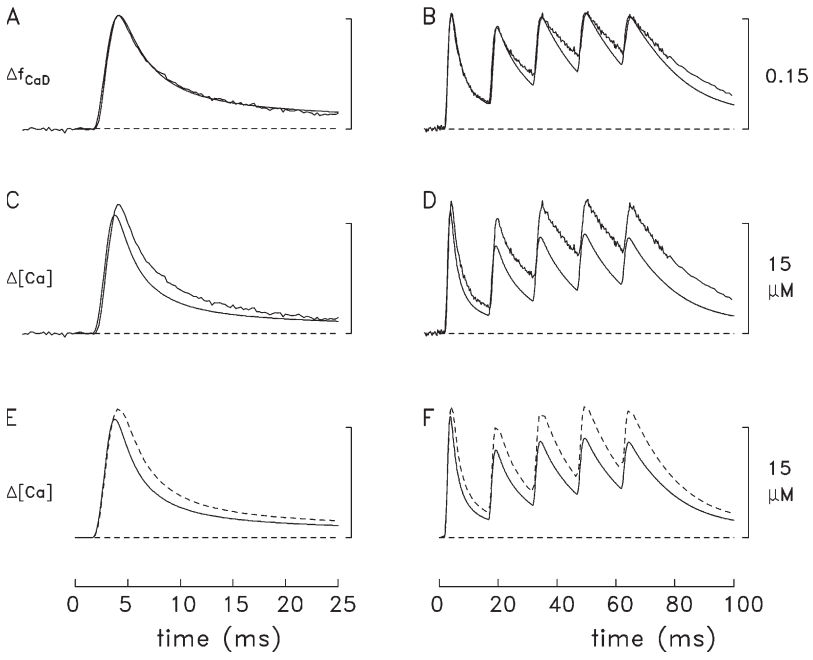

Figure 4. Comparison of spatially averaged waveforms in the experiments and simulations. (A) superposition of the Δf_{CaD} waveforms in Fig. 3 C and Fig. 3 A (noise-free and slightly noisy traces, respectively). (C) Superposition of the $\Delta[Ca^{2+}]$ waveform in Fig. 3 C (noise-free trace) and the $\Delta[Ca^{2+}]$ waveform in Fig. 3 A (noisy trace). (E) Superposition of the $\Delta[Ca^{2+}]$ waveform in Fig. 3 C (continuous trace) and $\Delta[Ca^{2+}]$ calculated with Eq. 3 from the Δf_{CaD} waveform in Fig. 3 C (dashed trace). (B, D, and F) Similar presentation for the measurements and simulations in Fig. 3 (B and D).

simulation results with the 18-compartment model. In each of these panels, the top two traces are the simulated waveforms of spatially averaged Δf_{CaD} and $\Delta[Ca^{2+}]$, respectively. The bottom trace is the SR Ca^{2+} release flux used to drive the simulations (described in Materials and Methods).

Fig. 4 (A and B) shows a comparison of the experimental and simulated Δf_{CaD} waveforms in Fig. 3. Good agreement is observed between these waveforms. This is one of the central results of this article and shows that the reaction-diffusion equations of spark Model 3, which was developed for frog fibers (Hollingworth et al., 2006), work well on this time scale when adapted to mouse fast-twitch fibers activated by APs. Columns 2 and 3 of Table IV give additional information about the amplitude and time course of the waveforms in Fig. 3 (A and C). The values of peak amplitude and FDHM of Δf_{CaD} are 0.155 and 5.3 ms, respectively, in the measurements and 0.155 and 5.1 ms in the simulations.

Fig. 4 (C and D) shows a comparison of two versions of spatially averaged $\Delta[Ca^{2+}]$. The noise-free waveforms are those in Fig. 3 (C and D), i.e., are the result of the 18-compartment simulations. The slightly noisy waveforms are those in Fig. 3 (A and B), i.e., are the single-compartment estimates of spatially averaged $\Delta[Ca^{2+}]$ calculated with Eq. 3 from the measured Δf_{CaD} signals. While these waveforms are generally similar, the estimates from the measurements are larger than the simulated $\Delta[Ca^{2+}]$ waveforms, and the difference is proportionally larger at later times.

The traces in Fig. 4 (E and F) reveal that the difference in the waveforms in Fig. 4 (C and D) is due to an error associated with the single-compartment method for estimating $\Delta[Ca^{2+}]$. The continuous traces in Fig. 4 (E and F) are the same as the simulated traces in Fig. 4 (C and D), i.e., are the "true" spatially averaged $\Delta[Ca^{2+}]$ waveforms as determined in the multicompartment simulations. The dashed traces are the single-compartment estimates of spatially averaged $\Delta[Ca^{2+}]$ based on the simulated Δf_{CaD} waveforms in Fig. 4 (A and B) and Eq. 3. This comparison reveals that the single-compartment method overestimates $\Delta[Ca^{2+}]$. The error arises from the assumption, inherent in a single-compartment model, that $\Delta[Ca^{2+}]$ is homogenous throughout the sarcomere. However, the multicompartment simulations reveal highly nonuniform changes, particularly at times during and immediately after Ca^{2+} release (Figs. 5 and 6, described below). As noted in the last section of Materials and Methods, the large $\Delta[Ca^{2+}]$ in and near the release compartment produces substantial nonlinearities in furaptra's response that vary with time. As a result, it is not possible to accurately calibrate the entire $\Delta[Ca^{2+}]$ waveform from Δf_{CaD} based on Eq. 3 and a single value of K_D.

Simulated Changes in the Individual Compartments

Fig. 5 shows spatially resolved (i.e., compartment) information from the 1-AP simulation of Fig. 3 C. Panel A shows $\Delta[Ca^{2+}]$ in the 18 compartments as a function of time. In this panel, the largest trace shows $\Delta[Ca^{2+}]$ in the release compartment and the next two largest traces show $\Delta[Ca^{2+}]$ in the intermediate and inner radial compartments at the longitudinal location of the release compartment. The three dashed traces (not all of which are distinguishable) show similar information at the longitudinal location adjacent to the z-line. The next four triplets of traces show this information at the other four longitudinal locations; in three of these four locations, no radial differences are discernable.

TABLE IV

Comparison of Measured and Simulated Spatially Averaged Waveforms Elicited by one AP (16 °C)

1	2	3	4	5
	peak amplitude	FDHM (ms)	peak amplitude	FDHM (ms)
A. Measurements				
furaptra Δf_{CaD}	0.155	5.3	0.178	6.8
furaptra $\Delta[Ca^{2+}]$	17.5 μM	4.5	20.8 μM	6.0
B. 18-Compartment simulations				
furaptra Δf_{CaD}	0.155	5.1	0.178	7.3
$\Delta[Ca^{2+}]$	16.1 μM	3.6	19.1 μM	4.8
Ca^{2+} release flux	205 μM/ms	1.6	227 μM/ms	1.6
$\Delta[Ca_{Total}]$	349 μM	–	386 μM	–

The values in columns 2 and 3 were determined from the measurements and simulations in Fig. 3 (A and C); those in columns 4 and 5 were determined from the measurements and simulations in Fig. 10 in response to the conditioning AP. $\Delta[Ca_{Total}]$ is the time integral of the release flux.

The traces in the other panels in Fig. 5 follow a similar pattern. The largest responses are found in the release compartment, and responses in the other compartments decline with distance from the release compartment; the dashed traces denote responses in the compartments next to the z-line. These other panels show changes in the concentration of Ca^{2+} bound to furaptra (Δ[CaDye]; B), troponin (Δ[CaTrop]; C), parvalbumin (Δ[CaParv]; D), and the SR Ca^{2+} pump (Δ[CaPump]; E). Panel F shows the concentration of released Ca^{2+} returned to the SR by the transport step of the Ca^{2+} pump (Δ[CaPumped]). Not shown are the changes in Ca^{2+} binding to ATP (Δ[CaATP]) in the 18 compartments. The time courses of these waveforms are very similar to those of $\Delta[Ca^{2+}]$ in the corresponding compartment (panel A). The amplitudes of the Δ[CaATP] and $\Delta[Ca^{2+}]$ waveforms are related by empirical factors that vary slightly with compartment location. For example, with 1 AP, peak Δ[CaATP] in the release compartment is 3.0 times peak $\Delta[Ca^{2+}]$ (240 and 80 μM, respectively). In the compartment farthest from the release compartment, peak Δ[CaATP] is 3.7 times peak $\Delta[Ca^{2+}]$ (10.54 and 2.85 μM, respectively). In the other compartments, peak Δ[CaATP] is between 3.4 and 3.8 times peak $\Delta[Ca^{2+}]$. Fig. 6 shows analogous spatially resolved information for the 5-AP simulation of Fig. 3 D.

The large gradients in $\Delta[Ca^{2+}]$, in combination with the differing reaction schemes in Fig. 2 and the differing diffusion constants in Table III (B) generate the variety of waveforms in the panels of Figs. 5 and 6. With troponin, which binds Ca^{2+} relatively quickly, differences among the compartments occur primarily at time <10 ms. With parvalbumin and the SR Ca^{2+} pump, the differences persist for longer times. Of importance for activation of the myofilaments, peak Δ[CaTrop] in response to both 1 and 5 APs is large in all troponin-containing compartments, ≥210 μM. Thus, peak occupancy is ≥0.88 times the concentration of Ca^{2+}-free troponin sites at rest, 239.3 μM (=240 μM minus the resting occupancy, 0.7 μM; see Table I and Fig. 1, legend).

Progressive Changes during High-Frequency Stimulation

According to the simulations in Fig. 3 D, the first AP in a 67-Hz train of APs releases ~350 μM total $[Ca^{2+}]$ ($\Delta[Ca_{Total}]$), whereas APs 2–5 in the train release 0.25–0.15 times the first release. The large reduction in release with subsequent APs in the train is probably due to Ca^{2+} inactivation of Ca^{2+} release (Baylor et al., 1983; Schneider and Simon, 1988; Jong et al., 1995) produced by the rise in myoplasmic $[Ca^{2+}]$ caused by the prior release(s).

It is possible that myoplasmic Ca^{2+} buffering due to the presence of 100 μM furaptra increases SR Ca^{2+} release above its normal value by reducing $\Delta[Ca^{2+}]$ and thus Ca^{2+} inactivation of Ca^{2+} release. This possibility was explored in simulations with 0 and 100 μM furaptra. According to these simulations, the peak of $\Delta[Ca^{2+}]$ in the release compartment (compare Fig. 1 A), which is likely to contain the receptor for Ca^{2+} inactivation of Ca^{2+} release, is 86 μM without furaptra and 80 μM with 100 μM furaptra; the time course of $\Delta[Ca^{2+}]$ in this compartment is essentially identical with 0 and 100 μM furaptra. Any perturbation in SR Ca^{2+} release due to the 7% reduction in the peak of $\Delta[Ca^{2+}]$ is expected to be minor.

An interesting feature of the waveforms in Fig. 3 (B and D) is that the changes in Δf_{CaD} and $\Delta[Ca^{2+}]$ evoked by the individual APs in the train decay progressively more slowly at later times. This feature is quantified in Fig. 7. The circles and X's in panel A show measured and simulated values, respectively, of the rate constant characterizing the early decay of Δf_{CaD} plotted as a function of the time of AP stimulation during the train. As expected from the similarity of the measured and simulated Δf_{CaD} traces in Fig. 4 B, the circles and X's in Fig. 7 A have similar values at all time points. The largest reduction in the rate constants occurs between the first and second shocks in the train (Hollingworth et al., 1996).

The X points in Fig. 7 B show analogous rate constants for the simulated $\Delta[Ca^{2+}]$ waveform in Fig. 3 D. A smaller rate of decay of $\Delta[Ca^{2+}]$ is expected for later peaks in the train because the myoplasmic Ca^{2+} buffers will become progressively more saturated with Ca^{2+} during maintained activity; thus, these buffers will become progressively less able to bind Ca^{2+} and assist in lowering free $[Ca^{2+}]$ after cessation of release (Melzer et al., 1986). Because furaptra responds rapidly to $\Delta[Ca^{2+}]$ and is heavily saturated with Ca^{2+} only near the release sites, the rate constants in Fig. 7 A are only ~20% smaller than the corresponding values in Fig. 7 B.

To quantify the decrease in the concentration of buffer sites available to bind Ca^{2+} during the train, the simulated concentration of sites that are free of bound ions shortly after each peak of Δf_{CaD}—and thus are immediately available to bind Ca^{2+} during the decay phase of

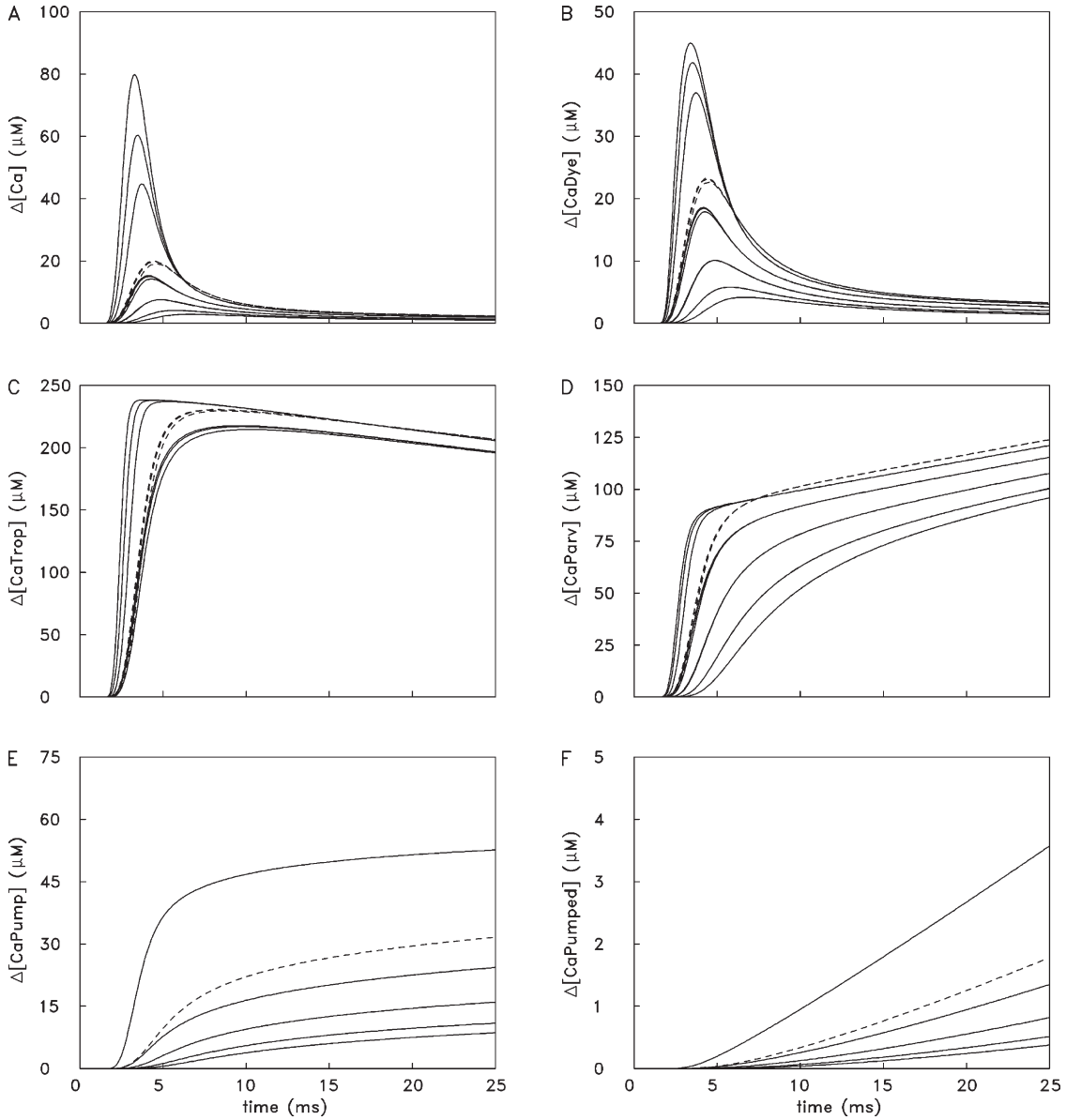

Figure 5. Ca^{2+} concentration changes in the 18 compartments in the simulation of Fig. 3 C. Δ[CaDye] includes both protein-free and protein-bound furaptra (Fig. 2 E); Δ[CaTrop] and Δ[CaPump] include the Ca^{2+} ions that are both singly and doubly bound to these buffers (Fig. 2, C and D). In each panel, peak amplitudes decline with distance from the release compartment; dashed traces denote changes in compartments adjacent to the z-line. In several panels, there is an apparent grouping of the traces in triplets, which corresponds to the three radial compartments at a given longitudinal location; at some longitudinal locations, the changes in the three radial compartments are indistinguishable. To facilitate comparisons among panels, the calibrations of the ordinates are referred to the total concentrations listed in Table I, which are spatially averaged. Because troponin and the Ca^{2+} pump are not located in all compartments, the simulated amplitudes of Δ[CaTrop] and Δ[CaPump] in their respective compartments are larger than shown in the plots by the ratio of the total site concentrations in these compartments to the spatially averaged concentrations (see Fig. 1, legend).

Δf_{CaD}—were determined. The spatially averaged concentrations of these sites (denote [Site]) are plotted in Fig. 7 C for troponin, parvalbumin, and the Ca^{2+} pump (the more slowly reacting Ca^{2+} buffers) vs. the time of the corresponding AP stimulus during the train. These concentrations were determined at the time points that marked the beginning of the period during which the simulated rate constants in Fig. 7 (A and B) were estimated (see legend). Fig. 7 C shows that the [Site] values for troponin and parvalbumin but not the Ca^{2+} pump decrease substantially during the train.

Fig. 7 D shows the associated changes in Ca^{2+} binding by these buffers. The changes in the simulated values of Δ[CaTrop], Δ[CaParv], and Δ[CaPump] were determined between the starting and ending times (denoted t_1 and t_2, respectively) during which the simulated decay rate constants in A and B were estimated. These values (denoted $\Delta[\text{CaSite}](t_2) - \Delta[\text{CaSite}](t_1)$) are plotted in

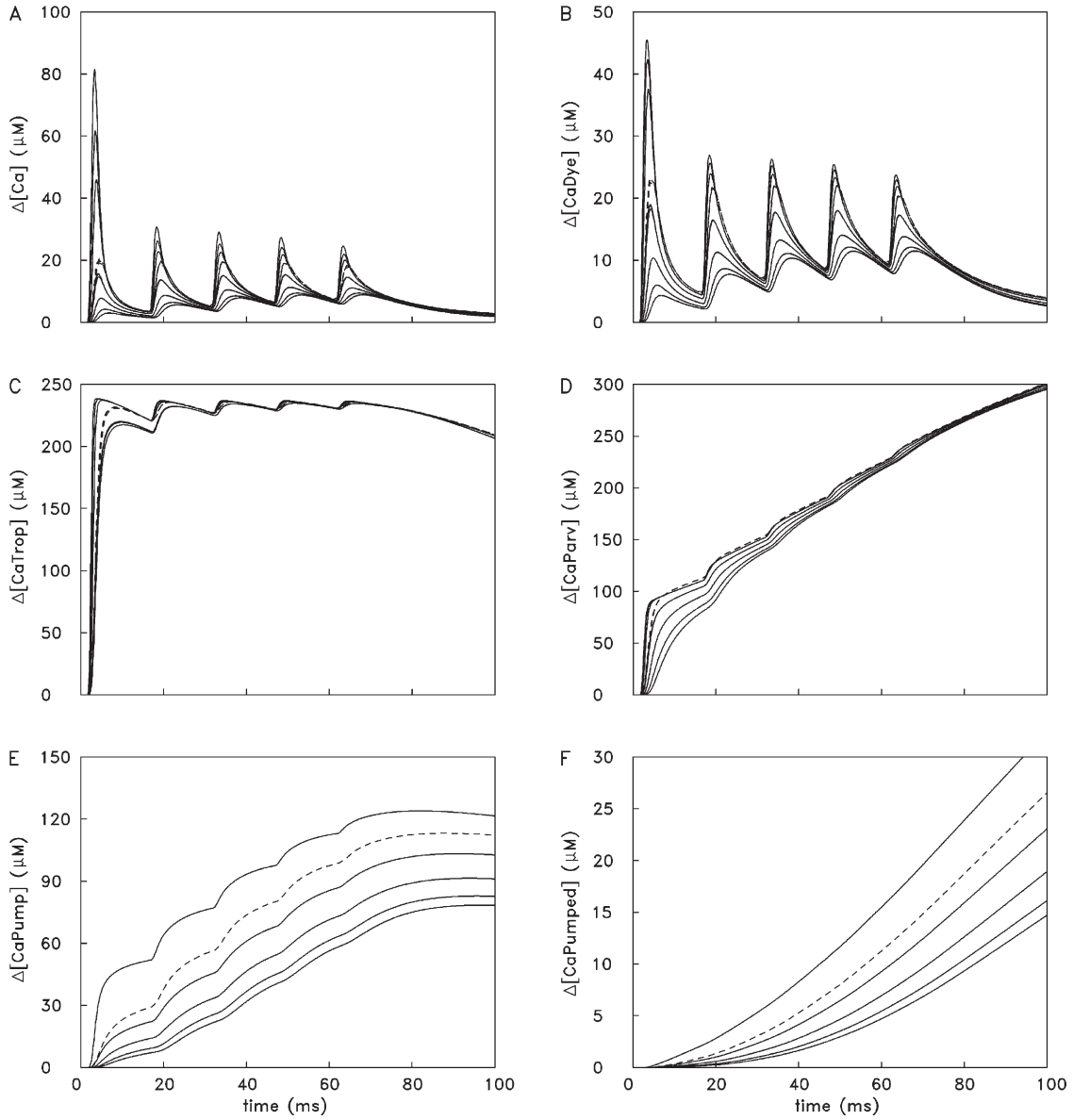

Figure 6. Ca^{2+} concentration changes in the 18 compartments in the simulation of Fig. 3 D. The presentation is like that in Fig. 5.

Fig. 7 D vs. the time of AP stimulation during the train. As expected from Fig. 7 C, the concentrations of Ca^{2+} bound by troponin and parvalbumin but not the pump decrease substantially during the train. (Note that ATP and furaptra respond rapidly to $\Delta[Ca^{2+}]$, and the values of $\Delta[\text{CaSite}](t_1) - \Delta[\text{CaSite}](t_2)$ for ATP and furaptra [not depicted] are negative rather than positive at all time points, i.e., ATP and furaptra release rather than bind Ca^{2+} between t_1 and t_2. Thus, decreased Ca^{2+} binding by ATP and/or furaptra does not underlie the decrease in the simulated rate constants in Fig. 7 (A and B). Also, the simulated concentration of Ca^{2+} transported by the Ca^{2+} pump progressively increases rather than decreases during the train (Fig. 6 F); thus, decreased transport of Ca^{2+} by the pump does not underlie the decrease in the simulated rate constants.)

Fig. 7 (C and D) indicates that a reduction in Ca^{2+} binding by troponin and parvalbumin but not the pump is primarily responsible for the decrease in the simulated rate constants in Fig. 7 (A and B) and presumably also in the measured rate constants in Fig. 7A.

The Effect of Parvalbumin on the FDHM of $\Delta[Ca^{2+}]$, Δf_{CaD}, and Δ[CaTrop]

Parvalbumin is thought to facilitate muscle relaxation in many types of fast-twitch muscle fibers (e.g., Gillis et al., 1982; Baylor et al., 1983; Rome et al., 1996). In twitch fibers of mice, the concentration of parvalbumin is strongly correlated with the fiber type (Heizmann et al., 1982; Ecob-Prince and Leberer, 1989). Slow-twitch fibers (type I) and fast glycolytic fibers (type IIa) have negligible and small-to-negligible concentrations, respectively;

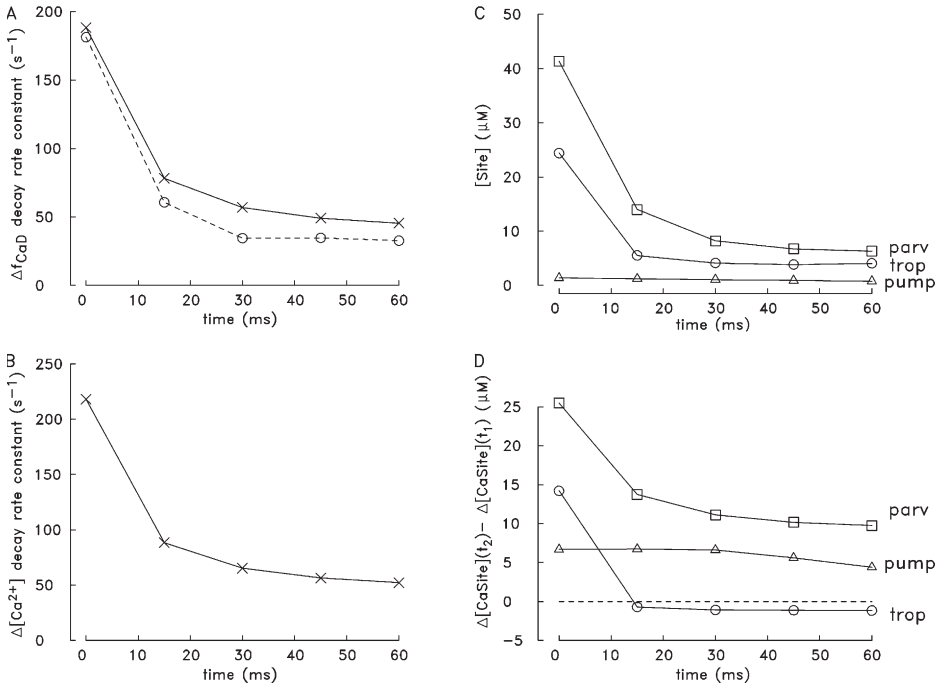

Figure 7. Analysis of changes in spatially averaged waveforms during a five-shock, 67-Hz stimulus (A, measurements; A–D, simulations). (A) The Δf_{CaD} waveforms in Fig. 3 (B and D) were analyzed to estimate the rate constants characterizing the early decay of the changes evoked by the five APs. For each change, a decaying single-exponential function without an offset was fitted to the falling phase of Δf_{CaD} during a 4–5-ms period that began 1–1.5 ms after peak; the time points that specify the beginning and end of each fitting period are denoted t_1 and t_2. The fitted rate constants are plotted vs. the times of the corresponding external shocks (open circles, measurements; X's, simulations). (B) Repeat of the analysis in A for the $\Delta[Ca^{2+}]$ waveform in Fig. 3 D; for each evoked change, rate constants were again determined between t_1 and t_2. (C) [Site] denotes the simulated spatially averaged concentration of sites on troponin (circles), parvalbumin (squares), and the Ca^{2+} pump (triangles) that are not bound with Ca^{2+}, Mg^{2+}, or H^+ at time t_1; the values were determined from the simulations for each of the five evoked changes. (D) Simulated values of Δ[CaSite](t_2) − Δ[CaSite](t_1), defined as the change in the spatially averaged concentration of Ca^{2+} bound to troponin (circles), parvalbumin (squares), and the pump (triangles) between times t_1 and t_2. As in C, the values were determined from the multicompartment simulations for each of the five evoked changes.

in contrast, fast oxidative-glycolytic fibers (type IIb) generally have large parvalbumin concentrations, comparable to that found in frog twitch fibers (Table I). In mouse EDL muscle, whose fiber-type composition is reported to be ~60% type IIb and ~40% type IIa (Ecob-Prince and Leberer, 1989), the average parvalbumin concentration is 4.4 g/kg wet weight (Heizmann et al., 1982). This corresponds to a myoplasmic concentration of Ca^{2+}/Mg^{2+} sites of ~1.26 mM, as calculated from (a) parvalbumin's molecular weight (~12,000), (b) the presence of two Ca^{2+}/Mg^{2+} sites per parvalbumin molecule, and (c) the factor 1/0.58 to convert a kilogram of muscle wet weight to a liter of myoplasmic water (Baylor et al., 1983). The value 1.26 mM is close to the standard parvalbumin site concentration in our simulations, 1.5 mM (Table I). If parvalbumin is present exclusively in the type IIb fibers of EDL muscle, the concentration of parvalbumin sites in these fibers could be ~2 mM. Because the parvalbumin concentration is reported to vary widely between type IIa and type IIb fibers, it was of interest to compare simulation results with different concentrations of parvalbumin sites (denoted $[Parv_{Total}]$).

In these simulations, $[Parv_{Total}]$ was varied between 0 and 2,000 μM. At each concentration, the amplitude of the release flux (set by the value of R in Eq. 1) was adjusted so that peak Δf_{CaD} was 0.155, the same as in Fig. 3 (A and C); the values of the total concentration of released Ca^{2+} varied from 298 μM (for $[Parv_{Total}] = 0$) to 365 μM (for $[Parv_{Total}] = 2{,}000$ μM). Fig. 8 shows the relations between $[Parv_{Total}]$ and the values of FDHM of spatially averaged $\Delta[Ca^{2+}]$ (squares), Δf_{CaD} (circles), and Δ[CaTrop] (X's). An increase in $[Parv_{Total}]$ from 0 to 2,000 μM produces a large reduction in all three FDHMs; by 61%, 74%, and 83%, respectively. As expected from the constraint of a constant peak Δf_{CaD}, much smaller changes were observed for peak $\Delta[Ca^{2+}]$ and peak Δ[CaTrop], +9% and −2%, respectively. These results supply a multicompartment confirmation that Ca^{2+} binding by parvalbumin is expected to shorten the duration of the twitch by abbreviating the time that $\Delta[Ca^{2+}]$ is elevated above the contractile threshold (Gillis et al., 1982) and hence abbreviating the time of thin filament activation, which is roughly proportional to the FDHM of Δ[CaTrop].

From Fig. 8, a $[Parv_{Total}]$ of ~1,400 μM is associated with an FDHM of Δf_{CaD} of 5.3 ms, the experimental value in Fig. 3 A (column 3 of Table IV, A). Interestingly, the values of FDHM of Δf_{CaD} measured in rested EDL fibers all fall in a reasonably narrow range, 3.7– 6.8 ms (mean ± SD = 5.4 ± 1.0 ms, n = 11; Hollingworth et al., 1996; Baylor and Hollingworth, 2003; see also Fig. 9, described in the next section). These values, in combination with Fig. 8, suggest that $[Parv_{Total}]$ was substantial in all of our EDL fibers, ≥800 μM, and therefore that all of these fibers were type IIb. Although, as noted above, ~40% of mouse EDL fibers are reported

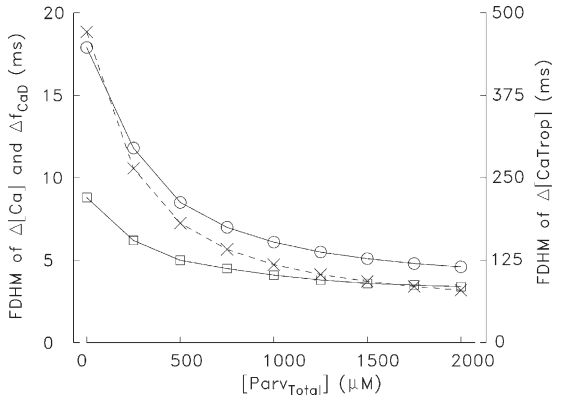

Figure 8. Effect of $[Parv_{Total}]$ (the total concentration of the Ca^{2+}/Mg^{2+} sites on parvalbumin) on the values of FDHM of spatially averaged Δf_{CaD} and $\Delta[Ca^{2+}]$ (circles and squares, respectively, calibrated on the lefthand ordinate) and of spatially averaged Δ[CaTrop] (X points, calibrated on the righthand ordinate) in the multicompartment simulations. At each value of $[Parv_{Total}]$, the value of R in Eq. 1 was adjusted to give peak Δf_{CaD} = 0.155, the value in column 2 of Table IV, A; no changes were made to other simulation variables.

to be type IIa, in which $[Parv_{Total}]$ is much smaller, these fibers may not have been sampled in our experiments. Our experiments are always performed on fibers located peripherally on the most distal head of the EDL muscle (Hollingworth et al., 1996). In mouse semimembranous muscle, which has 80–90% type IIb fibers, the fibers at the periphery of the muscle are reported to have larger parvalbumin concentrations than the fibers near the center (Ecob-Prince and Leberer, 1989).

$[Ca^{2+}]_R$ and the Relation between the Peak and FDHM of Δf_{CaD}

The open symbols in Fig. 9 show the experimental values of FDHM of Δf_{CaD} plotted vs. the peak amplitude of Δf_{CaD} for the 11 fibers of this study when stimulated by one AP. The FDHM values range from 3.7 to 6.8 ms (mentioned above) and the Δf_{CaD} amplitudes range from 0.141 to 0.184. While the relation between these data is somewhat noisy, the data appear to be positively correlated. It was therefore of interest to see if simulations like those in Fig. 3 C, but with many different values of R in Eq. 1, revealed a positive correlation between these parameters. The continuous curve in Fig. 9 shows the simulated relation between the peak and FDHM of Δf_{CaD} at the standard values of $[Ca^{2+}]_R$ and $[Parv_{Total}]$, 50 nM and 1,500 mM, respectively (Table I). The top and bottom dashed curves were obtained with similar simulations but with values of $[Ca^{2+}]_R$ of 150 and 0 nM, respectively. Over the range of measured Δf_{CaD} amplitudes, all curves reveal a positive correlation between the peak and FDHM of Δf_{CaD}, similar to that in the data.

The relation in Fig. 9 was also simulated at $[Ca^{2+}]_R$ = 50 nM with values of $[Parv_{Total}]$ of 1,000 and 2,000 μM (not depicted). Compared with the continuous curve in Fig. 9, these relations are shifted to higher and lower values on the ordinate, respectively. These effects of $[Ca^{2+}]_R$ and $[Parv_{Total}]$ on the simulated relation are reasonable because increases/decreases in $[Ca^{2+}]_R$ will decrease/increase the concentration of metal-free sites available on parvalbumin, which will increase/decrease FDHM of Δf_{CaD} (Figs. 7 and 8).

The explanation of the failure of the data points in Fig. 9 to lie on a single curve includes one or more of the following: fiber-to-fiber variation in $[Ca^{2+}]_R$, fiber-to-fiber variation in $[Parv_{Total}]$, and noise in the experimental determination of peak and FDHM of Δf_{CaD}. Overall, the data are generally consistent with $[Ca^{2+}]_R$ = 50 nM and $[Parv_{Total}]$ = 1,500 μM, as used in the standard simulation conditions (continuous curve).

Recovery of SR Ca^{2+} Release after a Conditioning Stimulus

Changes in the amount of SR Ca^{2+} release and changes in the decay phase of Δf_{CaD} subsequent to a first stimulus were described above in connection with Fig. 3 (B and D) and Fig. 7. This section describes measurements with a two-pulse protocol that was used to study the ability of the fiber to recover from the effects of a first stimulus. In this protocol, a first AP elicits a first Ca^{2+} release; then, after a variable waiting period, a second AP elicits a second release. Analysis of the amplitudes of the associated release fluxes is expected to give information about recovery of the release system from Ca^{2+} inactivation of Ca^{2+} release (e.g., Jong et al., 1995). The analysis is also expected to give information (described in the next section) about the time required for the slowly reacting myoplasmic Ca^{2+} buffers to recover their ability to bind Ca^{2+} and thus speed the decay of Δf_{CaD}.

The two-AP protocol was performed in three fibers, all of which were at a sarcomere length of 4.0 μm. Five common waiting periods between pulses were used in these experiments: 40, 80, 160, 320, and 400 ms; in addition, in two of the three experiments, a 15-ms waiting period was used. The top superimposed traces in Fig. 10 A show the averaged Δf_{CaD} signals recorded with the five common waiting periods. The Δf_{CaD} amplitudes evoked by the second stimulus are smaller than that evoked by the conditioning stimulus, and the FDHM values are larger; with time, these values recover toward those of the conditioning stimulus. In some of the records, a small movement artifact is apparent during the later falling phase of the Δf_{CaD} evoked by the conditioning stimulus, as indicated by a slight undershoot of the baseline (time of peak undershoot ≈ 90 ms). The time course of the movement artifact appeared to be similar to the time course of twitch tension (unpublished data), as both the tension transient and the undershoot of Δf_{CaD} returned to baseline with very similar time courses. The tension transient was therefore used to correct for the movement artifact in Δf_{CaD}. To do so, the tension transient was inverted and scaled so that its time course

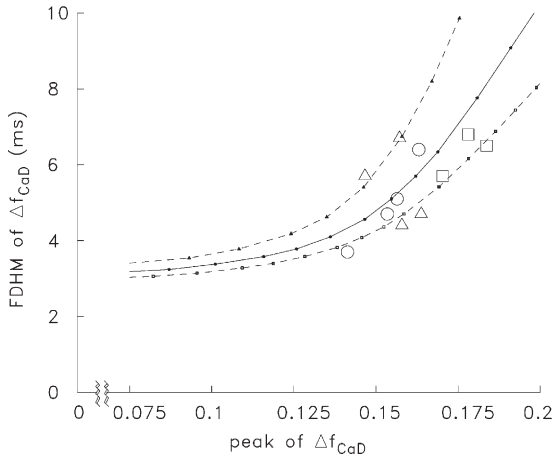

Figure 9. Relation between the peak amplitude and FDHM of spatially averaged Δf_{CaD} in the measurements and simulations. The large symbols show results from 11 rested EDL fibers stimulated by a single AP; circles, squares, and triangles give the values from the four fibers of Fig. 3 (A and B), the three fibers of Fig. 10 A, and the remaining fibers of this study, respectively. The curves through the small filled symbols show the relations determined in the multicompartment simulations with many values of R in Eq. 1 at three values of $[Ca^{2+}]_R$: 150 nM (top curve), 50 nM (the standard value in the simulations; middle curve), and 0 nM (bottom curve). For the middle curve, the range in release fluxes that corresponds to the range in the experimental amplitudes of Δf_{CaD} is 191–233 μM/ms.

during the period 90–250 ms matched that of the negative phase of Δf_{CaD}; the scaled tension transient was then subtracted from each of the Δf_{CaD} waveforms. The corrected waveforms are shown as the bottom superimposed traces in Fig. 10 A.

The Δf_{CaD} waveforms evoked by the conditioning stimulus ($t = 0$ ms) are similar in all recordings; the mean ± SD values of the peak amplitude and FDHM of this Δf_{CaD} are 0.178 ± 0.003 and 6.8 ± 0.4 ms, respectively ($n = 5$; columns 4 and 5 of Table IV, A). The circles in Fig. 11 A show the normalized amplitude of this and the other Δf_{CaD} responses in Fig. 10 A plotted as a function of the time of stimulation. For this plot, each amplitude was determined as its peak amplitude minus its starting value on Δf_{CaD} evoked by the conditioning stimulus (not its peak relative to baseline), and each amplitude was divided by that evoked by the conditioning pulse (filled circle). The small circle in Fig. 11 A shows the normalized amplitude with a waiting period of 15 ms between APs, which was obtained from the averaged responses in the two experiments with this measurement. With a brief waiting period between APs, the amplitude of the second Δf_{CaD} is smaller than that of the first; with longer waiting periods, the amplitude of the second Δf_{CaD} approaches that of the first.

Fig. 10 B shows results of simulations designed to mimic the experimental results in Fig. 10 A. The top superimposed traces show the simulated Δf_{CaD} waveforms obtained with the five common waiting periods; the bottom superimposed traces show the associated Ca^{2+} release waveforms. As usual, the amplitudes of the release fluxes were chosen so that the peaks of the simulated Δf_{CaD} waveforms (relative to baseline) matched the experimental ones. The Δf_{CaD} waveforms in Fig. 10 B appear to reproduce qualitatively the main features of the experimental Δf_{CaD} waveforms. The normalized amplitudes of the simulated Δf_{CaD} responses are shown as the X's in Fig. 11 A, which are similar to those of the measurements (circles).

The triangles in Fig. 11 A show the amplitudes of the release fluxes in the simulations, normalized by that of the conditioning release. The amplitudes of the second releases increase progressively from 0.239 ($t = 15$ ms) to 0.917 ($t = 400$ ms) times that of the first release. The triangles at $t \geq 40$ ms have been fitted with a decaying single-exponential function having three adjustable parameters: an initial value, a final value, and a rate constant (see legend). The points are well fitted by this function (continuous curve in Fig. 11 B); the curve also intersects the point at $t = 15$ ms, which was not included in the fit. According to the curve, the large reduction in release after the first AP recovers to 0.97 of the initial release with a rate constant of 6.9 s^{-1} (time constant of 146 ms). If the receptor site for Ca^{2+} inactivation of Ca^{2+} release has a dissociation constant for Ca^{2+} that is large compared with the values of $[Ca^{2+}]$ at times ≥40 ms, the dissociation rate constant of Ca^{2+} from this site should be ~6.9 s^{-1}. On the other hand, if the K_D of the receptor site is small, the dissociation rate constant may be larger than 6.9 s^{-1}.

Recovery of the Fast Decay of Δf_{CaD} after a Conditioning Stimulus

In Fig. 10 A, the five waveforms evoked by the second AP differ in time course as well as in amplitude. With a short delay between stimuli, the decay of the second Δf_{CaD} is markedly slower than that of the conditioning stimulus (compare Fig. 7 A); with longer delays, the decay becomes faster and approaches that of the conditioning stimulus. Similar changes are observed in the simulated waveforms (Fig. 10 B).

The simulations were analyzed to determine what changes in Ca^{2+} binding by the slow Ca^{2+} buffers are associated with recovery of the fast decay of Δf_{CaD}. The circles in Fig. 11 B plot the decay rate constants of the individual Δf_{CaD} measurements in Fig. 10 A; as in Fig. 11 A, Fig. 11 B also includes the data point at $t = 15$ ms (small circle). The X's in Fig. 11 B plot the decay rate constants of the simulated Δf_{CaD} responses. Both plots reveal that the decay rate constant at $t = 15$ and 40 ms is substantially smaller than that at $t = 0$ ms and, as time increases, the rate constant recovers toward the initial value. There are some discrepancies, however, between the simulated and measured rate constants. The simulated value

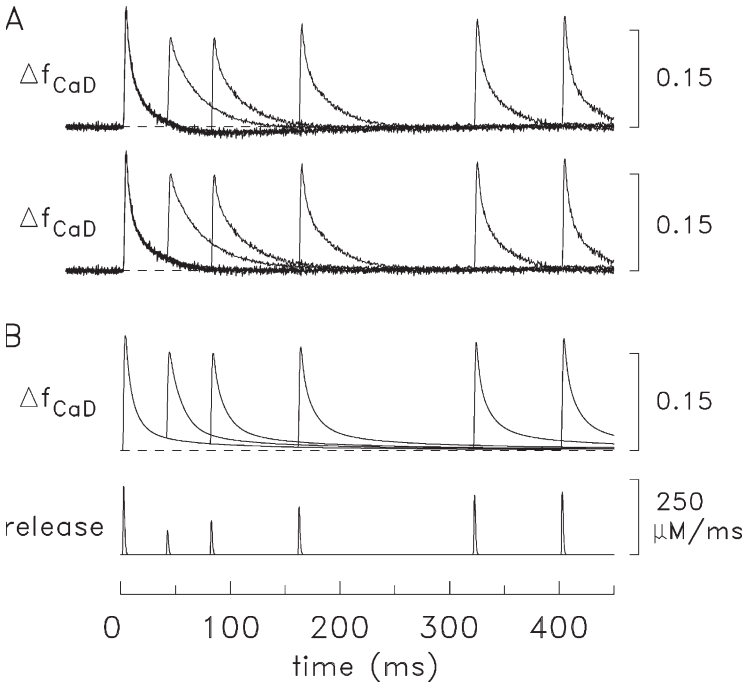

Figure 10. Spatially averaged Δf_{CaD} responses with a two-AP protocol with waiting periods of 40, 80, 160, 320, and 400 ms between APs. (A) Δf_{CaD} responses averaged from three EDL fibers (top) and these responses after correction for a small movement artifact by the method described in the text (bottom). A rest period of 1 min was used between repetitions of the paired stimuli. Fiber identification numbers: 021097.1, 042597.1, and 042597.2. (B) Top: simulated multicompartment Δf_{CaD} responses to mimic the lower traces in A; bottom: the Ca^{2+} release waveforms used to drive the simulations. The release flux amplitudes are 227 μM/ms for the conditioning stimulus and 0.358, 0.498, 0.703, 0.871, and 0.917 times that of the conditioning pulse (waiting periods of 40, 80, 160, 320, and 400 ms, respectively).

for the conditioning stimulus, 132 s^{-1} ($t = 0$ ms), is not as large as the measured value, 150 s^{-1}, and the simulated values between 15 and 320 ms are all noticeably larger than the measured values. The precise reason(s) for these differences is not known.

Another difference between the simulated and measured rate constants in Fig. 11 B is that the recovery of the simulated rate constant slows at late times and the measured value overtakes the simulated value. A possible explanation for this discrepancy is that $\Delta[Ca^{2+}]$ evoked by the conditioning AP returns to baseline less rapidly in the simulations than in the measurements, thus delaying the recovery of parvalbumin; for example, at $t = 400$ ms, simulated spatially averaged $\Delta[Ca^{2+}]$ in response to the conditioning AP is 108 nM above resting. A slower return of $\Delta[Ca^{2+}]$ could occur if the turnover rate of the Ca^{2+} pump in the simulations is smaller than the actual turnover rate, or if some other slow process or buffer not included in the simulations contributes to the actual decline of $\Delta[Ca^{2+}]$ on this time scale. As demonstrated in an earlier section ($[Ca^{2+}]_R$ and the Relation between the FDHM and the Peak of Δf_{CaD}), release fluxes that produce Δf_{CaD} waveforms with identical peak amplitudes are associated with larger values of FDHM of Δf_{CaD} (and hence smaller decay rate constants) if $[Ca^{2+}]_R$ is larger. The conclusion that $\Delta[Ca^{2+}]$ returns to baseline more slowly in the simulations than the measurements is supported by preliminary experiments with fluo-3, which can be used to follow the time course of the decline of $\Delta[Ca^{2+}]$ with much greater accuracy than is available with furaptra. These experiments indicate that $\Delta[Ca^{2+}]$'s return is indeed somewhat slower in the simulations than in the measurements (Baylor, S.M., and S. Hollingworth. 2007. *Biophys. J.* 92:311a). The reason for this shortcoming in the model merits further investigation.

Fig. 11 (C and D) (which is analogous to Fig. 7, C and D) shows the analysis of the simulated changes on troponin, parvalbumin, and the Ca^{2+} pump (the slowly reacting Ca^{2+} buffers) during the time periods when the decay rate constants in Fig. 11 B were estimated. As expected from Fig. 7 C, Fig. 11 C reveals that the conditioning AP produces a marked decline in the concentration of sites on troponin and parvalbumin, but not on the pump, that are immediately available to bind Ca^{2+} early in the falling phase of Δf_{CaD} in response to a release initiated 15 ms after the first release. Between 15 and 320–400 ms, the available site concentrations on troponin and parvalbumin, but not the pump, recover substantially. Fig. 11 D shows that a similar pattern is observed for the simulated concentrations of Ca^{2+} actually bound by troponin, parvalbumin, and the pump during the early decay of Δf_{CaD}. Presumably, recovery of the ability of troponin and parvalbumin to bind Ca^{2+} is primarily responsible for the reappearance of the fast decay rate of Δf_{CaD} in the measurements (Fig. 11 B, open circles).

Simulations at Sarcomere Length = 2.4 μm

To our knowledge, myoplasmic Ca^{2+} transients have not been measured in the same mammalian fibers at short- and long-sarcomere length. This is difficult to do on a bundle of intact fibers, only one of which contains a Ca^{2+} indicator (as in our experiments). We have therefore used simulations to estimate sarcomeric Ca^{2+} movements in mouse fast-twitch fibers at a physiological sarcomere length, 2.4 μm.

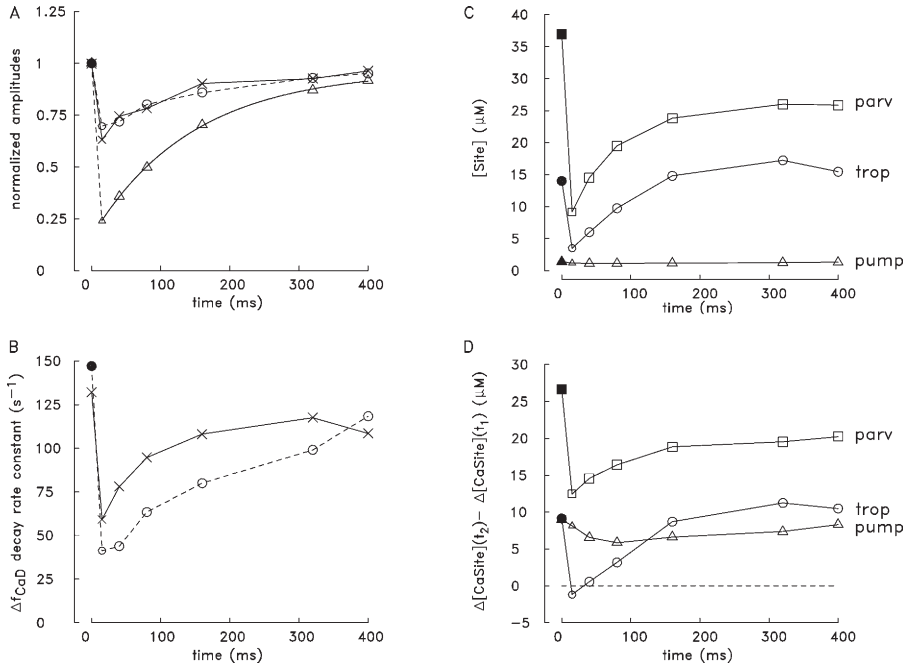

Figure 11. Analysis of measured and simulated responses with the two-AP protocol. (A) The large circles show the amplitudes of the measured Δf_{CaD} signals in Fig. 10 A (bottom traces) normalized by 0.178, the mean amplitude evoked by the conditioning stimulus (filled circle, $t = 0$ ms); each Δf_{CaD} amplitude was determined as the peak of Δf_{CaD} minus its starting value on the Δf_{CaD} trace evoked by the conditioning stimulus. The small circle at $t = 15$ ms shows the normalized amplitude averaged from the responses of the two fibers of Fig. 10 A that had measurements with a 15-ms waiting period between APs. The X's show similar information for Δf_{CaD} in the simulations of Fig. 10 B, as well as for a simulation with a 15-ms waiting period. The triangles show the amplitudes of the release fluxes in the simulations normalized by the release flux of the conditioning stimulus (227 μM/ms). The curve through the triangles is a least-squares fit of the points at $t \geq 40$ ms with the function $f(t) = R0 + (Rmax - R0) \cdot (1 - \exp(-r \cdot t))$. The fitted values of R0, Rmax, and r are 0.164, 0.965, and 6.87 s^{-1}, respectively. (B) Decay rate constants of Δf_{CaD} in the measurements (circles) and simulations (X's), determined as in Fig. 7 (A and B). (C and D) Values of [Site] and Δ[CaSite](t_2) − Δ[CaSite](t_1), determined as in Fig. 7 (C and D).

For these simulations, the 18-compartment arrangement (six longitudinal by three radial) was retained (Fig. 1 B), but five changes were implemented. (1) The half-sarcomere length (distance between the z- and m-lines) was shortened from 2.0 to 1.2 μm. (2) To keep the myoplasmic volume constant, the radius of the myofibril was increased from 0.375 to 0.484 μm (appropriate for a cylindrical geometry). (3) To match the thin-filament length of 1.0 μm (=5/6 of the new half-sarcomere length), the number of troponin-containing compartments was increased from 9 to 15; thus only the three compartments adjacent to the m-line lacked troponin. (4) To keep constant the spatially averaged concentration of troponin sites (240 μM, Table I), the troponin site concentration within the 15 compartments was set to 288 μM (vs. 480 μM at sarcomere length = 4.0 μm; see Fig. 1, legend). (5) The Ca^{2+} release compartment was moved from the second to the third compartment in the outer longitudinal row, so that the location of Ca^{2+} release would remain at the middle of the thin filament (0.5 μm from the z-line). Not changed in these simulations was the Ca^{2+} release function evoked by an AP, which remained as in Fig. 3 C.

Fig. 12 A compares simulated spatially averaged waveforms at a sarcomere length of 2.4 μm (dashed traces) and 4.0 μm (continuous traces). The top pair of traces shows Δf_{CaD} and the bottom pair shows $\Delta[Ca^{2+}]$. The Δf_{CaD} waveforms are noticeably different, although, somewhat surprisingly, the $\Delta[Ca^{2+}]$ waveforms are almost identical. The peak amplitude of Δf_{CaD} is 17% larger at short-sarcomere length (0.182 vs. 0.155), FDHM is 16% smaller (4.3 vs 5.1 ms), and the time of peak is 5% smaller (3.9 vs. 4.1 ms). These differences arise because, as noted in the next paragraph, better mixing of Ca^{2+} among the compartments occurs at short-sarcomere length.

An analysis of the Ca^{2+}-buffer responses in the 18 compartments (compare Fig. 5) revealed qualitatively similar changes at short- and long-sarcomere length. For any particular buffer, the most obvious change in the compartment waveforms was that the difference between the smallest and largest peak values was usually smaller at short-sarcomere length. For example, the peaks of the $\Delta[Ca^{2+}]$ waveforms varied from 9 to 64 μM at sarcomere length of 2.4 vs. 3 to 80 μM at sarcomere length of 4.0 μm (Fig. 5 A); the peaks of Δ[CaATP] varied from 34 to 178 μM vs. 11 to 240 μM; and the peaks of Δ[CaDye] varied from 12 to 37 μM vs. 4 to 45 μM (Fig. 5 B). The greater extremes in the peak values at long-sarcomere length are expected from the greater diffusion distance to the m-line with a half-sarcomere length of 2.0 vs. 1.2 μm. An exception to this observation occurs with troponin, which is not distributed uniformly within the sarcomere. The peaks of the Δ[CaTrop] waveforms varied from 193 to 238 μM at short-sarcomere length vs. 215 to 238 μM at long-sarcomere length (Fig. 5 C). The larger range at short-sarcomere length appears to be due to the fact that although longitudinal diffusion distances to reach the troponin sites are similar at short-and long-sarcomere length, radial diffusion distances are larger at short-sarcomere length.

Fig. 12 B shows another comparison of simulated $\Delta[Ca^{2+}]$ waveforms at the two sarcomere lengths (dashed,

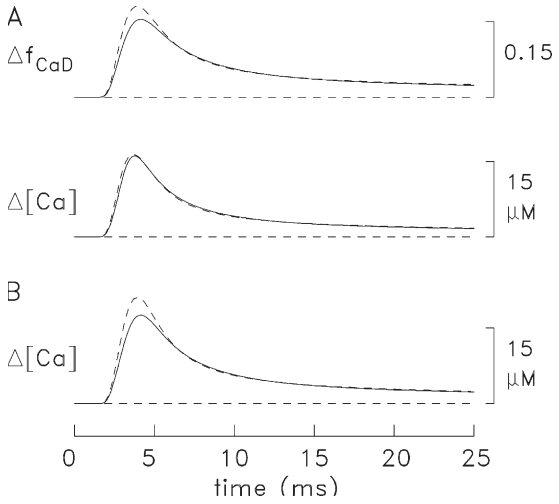

Figure 12. Simulations of spatially averaged responses evoked by one AP at sarcomere lengths of 2.4 μm (dashed traces) and 4.0 μm (continuous traces). (A) The top pair of traces shows Δf_{CaD} and the bottom pair $\Delta[Ca^{2+}]$, averaged over the 18 compartments. (B) Single-compartment estimates of $\Delta[Ca^{2+}]$ obtained with Eq. 3 from the Δf_{CaD} traces in A. The modifications of the model for the multicompartment simulation at sarcomere length = 2.4 μm are described in the text (see also Fig. 1 B). The Ca^{2+} release flux was identical to that in Fig. 3 C.

2.4 μm; continuous, 4.0 μm). These waveforms, rather than being the "true" spatially averaged $\Delta[Ca^{2+}]$ waveforms (Fig. 12 A), are the single-compartment estimates obtained with Eq. 3 from the (spatially averaged) Δf_{CaD} waveforms in Fig. 12 A (compare the dashed $\Delta[Ca^{2+}]$ traces in Fig. 4, E and F). The peak amplitude of the trace in Fig. 12 B at 2.4 μm is 20% larger than that at 4.0 μm (21.2 vs. 17.6 μM), FDHM is 16% smaller (3.8 vs. 4.5 ms), and time of peak is 5% smaller (3.9 vs. 4.1 ms). These differences are similar to those estimated with furaptra in experiments on frog single fibers at different sarcomere lengths, where the peak of $\Delta[Ca^{2+}]$ is ~25% larger at a sarcomere length of 2.5 than at 4.0 μm, FDHM is ~25% smaller, and time of peak is ~10% smaller (Konishi et al., 1991). Because SR Ca^{2+} release at long-sarcomere length and myoplasmic Ca^{2+} buffering appear to be similar in mouse fast-twitch fibers and frog twitch fibers (Table I and Baylor and Hollingworth, 2003), the combined results of the measurements and simulations suggest that the SR Ca^{2+} release waveforms evoked by an AP are quite similar at short- and long-sarcomere length.

Effect of the Location of the SR Ca^{2+} Release Sites Relative to the z-Line

Amphibians and mammals reveal a striking difference in the organization of the triadic junctions. In amphibians, the junctions occur once per sarcomere and are centered on z-lines; in mammals, they occur twice per sarcomere and are offset ~0.5 μm from the z-lines. This difference is expected to offer advantages to mammals for contractile activation; specifically, for a given Ca^{2+} release waveform, the binding of Ca^{2+} to troponin would be expected to be more uniform along the thin filament and, on average, occur more rapidly.

To explore this effect quantitatively, simulations at a sarcomere length of 2.4 μm (compare preceding section) were performed with two different Ca^{2+} release locations: the third compartment in the outer row (as for the simulations in Fig. 12) and the first compartment in the outer row (to simulate the location of the triadic junctions in amphibians). For these simulations, the furaptra concentration was set to 0 to eliminate any (small) effects of furaptra buffering on the results.

Fig. 13 shows simulated responses to 1 AP with the two Ca^{2+} release locations. Each panel shows a family of Δ[CaTrop] waveforms at five different distances from the z-line; the top and bottom panels correspond to the mammalian and amphibian release locations, respectively. To simplify the presentation, each of the displayed waveforms is an average of Δ[CaTrop] over the three radial compartments at one of the five longitudinal locations containing troponin. As expected, the waveforms in the top panel are more uniform in amplitude and time course than those in the bottom panel. In the top panel, peak amplitudes vary from 200 to 233 μM and times of peak from 6.0 to 11.3 ms; in the bottom panel, the corresponding ranges are 170 to 231 μM and 7.7 to 16.3 ms. In both panels, the waveform at the longitudinal location most distant from the z-line (which corresponds to the end of the thin filament) has both the smallest peak value and the largest time of peak. At this location, the peak value in the bottom panel, 170 μM, is only 0.71 times the maximum value (239.3 μM); the peaks of all other waveforms in Fig. 9 are ≥200 μM, which are ≥0.84 times maximum.

A high occupancy of troponin with Ca^{2+} near the end of the thin filament would appear to be particularly advantageous to fiber contraction, as this region of the thin filament is within reach of myosin cross-bridges at most working sarcomere lengths. Thus, the simulations demonstrate a clear advantage for contraction in locating the site of SR Ca^{2+} release at the middle of the thin filament rather than at the z-line. Another way to quantify this advantage is to determine the percentage increase in the amplitude of Ca^{2+} release at the z-line that would yield an average peak Δ[CaTrop] at the end of the thin filament of 200 μM (=the value simulated with one AP when release is located at the middle of the thin filament). This percentage increase, determined in additional simulations, is 8%. In this case, however, the time of peak Δ[CaTrop] at the end of the thin filament is 15.5 ms, which remains longer than the 11.3-ms value when release is located at the middle of the thin filament. Thus, locating Ca^{2+} release at the middle of the thin filament has the advantage of using a smaller release flux

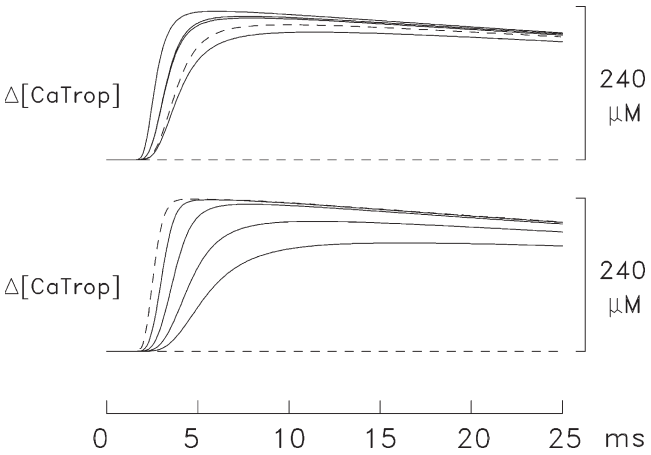

Figure 13. Simulated families of Δ[CaTrop] waveforms at a sarcomere length of 2.4 μm with two Ca^{2+} release locations: the middle of the thin filament (top) and adjacent to the z-line (bottom). These locations approximate the location of the triadic junctions in mammalian and amphibian fibers, respectively. Each waveform represents an average over the three radial compartments at one of the five longitudinal locations of the 15 troponin-containing compartments; these are centered at 0.1, 0.3, 0.5, 0.7, and 0.9 μm from the z-line. As in Fig. 5 C, Δ[CaTrop] includes changes in both the singly and doubly bound Ca^{2+} states of troponin, and the concentration change on the ordinate is referred to the entire myoplasmic volume. In each panel, the peak amplitudes decline with distance from the release compartment; the dashed trace shows the result closest to the z-line. The SR Ca^{2+} release function was identical to that in Fig. 3 C.

to achieve a faster and more uniform binding of Ca^{2+} along the length of the thin filament.

Possible Influence of Ca^{2+} Uptake by Mitochondria

The simulations of this article do not take into account uptake of Ca^{2+} by the mitochondria. In this section, we show that inclusion of mitochondrial Ca^{2+} uptake would have a negligible effect on the simulations of this article. Our analysis relies on three pieces of information in the literature. (1) In rat fast-twitch fibers at 37°C, the maximal rate of Ca^{2+} uptake by mitochondria is 65 nmol of Ca^{2+} per mg protein per min (Sembrowich, Quintinskie, and Li, 1985). If a Q_{10} of 2 is assumed, this corresponds to a maximal uptake rate at 16°C of ~16 nmol of Ca^{2+} per mg protein per min. (2) The protein content of mitochondria is 0.385 g per cm^3 (Schwerzmann, Hoppeler, Kayar and Weibel, 1989). (3) In rodent fast-twitch fibers, the estimated fraction of the fiber volume taken up by mitochondria is 2–8% (Eisenberg, 1983).

The maximal rate of mitochondrial Ca^{2+} uptake in rodent fast-twitch fibers at 16°C is thus estimated to be ~0.008 μM/ms if referred to the fiber volume, or ~0.012 μM/ms if referred to the myoplasmic water volume (compare Baylor et al., 1983). The latter value is <0.1% of the maximal SR Ca^{2+} release rates in Figs. 3 and 10 and <2% of the maximal rate of Ca^{2+} uptake by the SR Ca^{2+} pump in the reaction scheme of Table II (D), 0.831 μM/ms. Mitochondrial Ca^{2+} uptake is thus estimated to be very small compared with the Ca^{2+} movements reported in this article.

Comparisons between Multicompartment and Single-Compartment Simulations

Fig. 4 (E and F) shows that spatially averaged $\Delta[Ca^{2+}]$ cannot be accurately estimated at all times from the furaptra Δf_{CaD} signal and Eq. 3. As a result, single-compartment inferences about Ca^{2+} binding to the myoplasmic Ca^{2+} buffers (e.g., Baylor and Hollingworth, 2003) will necessarily have some errors, as will estimates of $\Delta[Ca_{Total}]$ and the Ca^{2+} release flux. Additional simulations were performed to estimate the magnitude of these errors. For these simulations, the dashed $\Delta[Ca^{2+}]$ traces in Fig. 4 (E and F) were used to calculate single-compartment waveforms of Δ[CaATP], Δ[CaTrop], Δ[CaParv], Δ[CaPump], and Δ[CaPumped] from the standard set of differential equations (compare the reaction schemes in Fig. 2); Δ[CaDye] was calculated from the Δf_{CaD} traces in Fig. 3 (C and D) with the relation $\Delta[CaDye] = \Delta f_{CaD} \times 100$ μM (the furaptra concentration in Table I). $\Delta[Ca_{Total}]$ was then calculated as the sum of $\Delta[Ca^{2+}]$, Δ[CaDye], Δ[CaATP], Δ[CaTrop], Δ[CaParv], Δ[CaPump], and Δ[CaPumped], and the release flux as the time derivative of $\Delta[Ca_{Total}]$.

As expected from the larger $\Delta[Ca^{2+}]$ traces in the single-compartment simulation (dashed traces in Fig. 4, E and F), the single-compartment estimates of $\Delta[Ca_{Total}]$ and the release fluxes were somewhat larger than the "true" values estimated in the 18-compartment simulation. With one AP, $\Delta[Ca_{Total}]$ at $t = 50$ ms was 14% larger in the single- vs. multicompartment simulation (398 vs. 349 μM), and, with 5 APs, $\Delta[Ca_{Total}]$ was 17% larger at 150 ms (754 vs. 647 μM). The peak and FDHM of the release waveform were also larger, 219 μM/ms and 1.7 ms vs. 205 μM/ms and 1.6 ms. The fractional reductions in Ca^{2+} release with APs 2–5 were very similar in both simulations. Thus, overall, the single-compartment estimates were in fair agreement with the multicompartment results.

These estimates of single-compartment errors in mouse fibers are somewhat smaller than those estimated previously in frog fibers (Baylor and Hollingworth, 1998), where SR Ca^{2+} release with single-compartment modeling was ~25% larger than that with multicompartment modeling. A smaller error in mouse fibers is expected from the fact that the location of SR Ca^{2+} release is offset from the z-line in mouse fibers. As noted in the preceding section, this offset is expected to reduce intrasarcomeric Ca^{2+} gradients and hence reduce the differences between single- and multicompartment modeling.

DISCUSSION

This article describes a multicompartment model for simulating Ca^{2+} movements within the sarcomere of

mouse fast-twitch fibers stimulated by APs. The implementation is based on a reaction-diffusion model developed recently for Ca^{2+} sparks in frog fibers (Hollingworth et al., 2006). The simulations were compared with spatially averaged Ca^{2+} transients measured in mouse EDL fibers with furaptra at 16°C (Hollingworth et al., 1996; Baylor and Hollingworth, 2003). Good agreement was observed between the simulated and measured furaptra Δf_{CaD} responses (Fig. 4, A and B, and Fig. 10). A clear strength of the model is its ability to simulate both large-scale Ca^{2+} movements of the type evoked here by APs and the small-scale Ca^{2+} movements that occur with Ca^{2+} sparks. The good agreement observed in these different settings should not be taken as good evidence that all model parameters are well known, however. It is clear that the choice of some parameter values can be "traded off" for others (e.g., $[Ca^{2+}]_R$ vs. the parvalbumin concentration; see Fig. 9) without significantly affecting the simulation results. Because good agreement between the simulations and measurements was observed in the initial calculations (Fig. 4, A and B), further refinement of model parameters to give better agreement with the measurements did not appear to be justified.

Figs. 5 and 6 confirm that large differences in $\Delta[Ca^{2+}]$ and in the concentration of Ca^{2+} bound to its buffers occur in different regions of the sarcomere for a number of milliseconds after AP-evoked SR Ca^{2+} release (compare Cannell and Allen, 1984; Baylor and Hollingworth, 1998; Novo et al., 2003). Substantial diffusive movements of Ca^{2+} and the mobile Ca^{2+} buffers (not directly illustrated in this article) result because of these gradients.

This article also estimated SR Ca^{2+} release and myoplasmic Ca^{2+} binding with a single-compartment model. The single-compartment model produced modest (10–20%) overestimates of the amount of SR Ca^{2+} release evoked by a single AP or a brief high-frequency train of APs. These overestimates arise because the single-compartment model cannot take into account the large gradients in $\Delta[Ca^{2+}]$ within the sarcomere (Fig. 5). The multicompartment model, however, has the disadvantage of added computational complexity. The choice of a single- vs. a multicompartment model for the analysis of a particular experiment needs to weigh the expected increase in accuracy of a multicompartment model vs. the computational simplicity of a single-compartment model. Some questions—e.g., what quantitative differences are expected to arise because of differences in sarcomere length (Fig. 12) or in the location of the triadic junctions (Fig. 13)—can only be addressed with a multicompartment model.

Properties of Ca^{2+} Release Evoked by a Single AP and a High-Frequency Train of APs

The good agreement between the simulated and measured Δf_{CaD} waveforms in Fig. 4 A and Fig. 10 supports the idea that, in a fast-twitch EDL fiber stimulated by one AP, the peak amplitude of SR Ca^{2+} release is 200–225 μM/ms and the FDHM of SR Ca^{2+} release is ~1.6 ms (16°C). The good agreement for a five-shock 67-Hz tetanus (Fig. 4 B) supports the conclusion that Ca^{2+} release in response to APs 2–5 declines progressively from ~0.25 to ~0.15 times that elicited by the first AP.

Ca^{2+} Inactivation of Ca^{2+} Release

The results indicate that the concentration of Ca^{2+} released by a second AP initiated 15 ms after a first AP is only ~0.25 times that evoked by the first (Figs. 3 and 10). This large reduction in release likely occurs because of Ca^{2+} inactivation of Ca^{2+} release produced by the rise in $[Ca^{2+}]$ elicited by the first release (compare Baylor et al., 1983; Schneider and Simon, 1988; Jong et al., 1995). The ability of the release system to recover from inactivation was studied with a two-AP protocol (Figs. 10 and 11). The results indicate that, during the period 15–400 ms after the first release, the amplitude of the second release recovers from ~0.25 to >0.9 times that of the first release with a rate constant of ~7 s^{-1}. This rate constant might reflect the ability of the release system to recover from inactivation uninfluenced by Ca^{2+}, as a large fraction of the recovery (0.36 to >0.9 times the first release) takes place ≥40 ms after the first release, when, according to the multicompartment simulation, $[Ca^{2+}]$ near the release sites is <2 μM.

The properties of Ca^{2+} inactivation of Ca^{2+} release in mouse fast-twitch fibers at 16°C have both similarities and differences when compared with those in frog cut fibers at 14–15°C (Jong et al., 1995). The relative amplitude of release with a second AP initiated ≤15 ms after the first is similar in the two preparations, ~0.3 times that of the first release, and the fractional recovery from inactivation after 200–400 ms is similar, >0.9. The values of the recovery rate constant, however, are different: ~7 s^{-1} in mouse fibers vs. ~40 s^{-1} in frog fibers. It is possible that the smaller value in mouse fibers is related, at least in part, to the time required for $\Delta[Ca^{2+}]$ to return to a sufficiently low level that the recovery rate constant becomes independent of Ca^{2+}. In the frog experiments, the myoplasm contained 20 mM EGTA, which is expected to quickly reduce $\Delta[Ca^{2+}]$ to <0.1 μM; thus, the rate constant reported for frog fibers is likely to be independent of Ca^{2+} (Jong et al., 1995). In the mouse fibers of this article, the return of $\Delta[Ca^{2+}]$ to a low level relies on the normal Ca^{2+} buffering and removal systems, and, as noted above, the simulations indicate that it takes ~40 ms for $[Ca^{2+}]$ near the release sites to fall below 2 μM. If this level is sufficiently low for recovery to proceed unaffected by Ca^{2+}, then the Ca^{2+}-independent recovery rate appears to be approximately sixfold smaller in mouse fibers than in frog fibers. It would be valuable to estimate this rate constant in mouse fibers with the EGTA or related method.

The Time Course of $\Delta[Ca^{2+}]$ Evoked by an AP

In EDL fibers stimulated by one AP, the value of FDHM of spatially averaged $\Delta[Ca^{2+}]$ is estimated to be 3.6–4.8 ms (16°C; Table IV, B). These small values depend on a brief Ca^{2+} release waveform and the presence of a substantial concentration of Ca^{2+} buffers in myoplasm that are capable of binding Ca^{2+} relatively quickly after cessation of release. The simulations indicate that both troponin and parvalbumin are major contributors to this Ca^{2+} binding. In fast-twitch mouse fibers, the concentration of Ca^{2+} regulatory sites on troponin is substantial, ~240 mM (Table I), and the simulations indicate that troponin captures Ca^{2+} during the falling phase of $\Delta[Ca^{2+}]$ (Figs. 5 and 7). In addition, type IIb EDL fibers have near millimolar concentrations of parvalbumin (Heizmann et al., 1982; Ecob-Prince and Leberer, 1989), and the simulations indicate that the Ca^{2+}/Mg^{2+} sites on parvalbumin also play an important role in binding Ca^{2+} during the falling phase of $\Delta[Ca^{2+}]$ (Figs. 5 and 7).

In frog twitch fibers having diameters similar to those of EDL fibers (30–50 μm), the average amplitude of the furaptra $\Delta[Ca^{2+}]$ signal elicited by one AP is very similar to that in EDL fibers (16.9 ± 1.5 and 17.8 ± 0.4 μM, respectively; estimated with Eq. 3) while its FDHM is larger (8.6 ± 1.6 and 4.6 ± 0.3 ms) (16°C; Hollingworth et al., 1996). If the concentrations and kinetics of the myoplasmic constituents are basically similar in these two fiber types (compare Tables I and II), the most likely explanation for the larger FDHM of $\Delta[Ca^{2+}]$ in frog fibers is that SR Ca^{2+} release lasts longer. A possible basis for such a difference is that frog fibers have an approximately equal mixture of RyR1 and RyR3 isoforms whereas EDL fibers have only the RyR1 isoform (see Introduction). Activity in the RyR3 isoform might underlie a broadening of the overall release time course. For example, it has been proposed that SR Ca^{2+} release in frog fibers involves activation of RyR1s by T-tubular depolarization, and the resultant rise in $[Ca^{2+}]$ then activates RyR3s via Ca-induced Ca^{2+} release (e.g., Klein et al., 1996; Shirokova and Rios, 1997; Gonzalez et al., 2000; see also Rios and Pizarro, 1988). It has not been ruled out, however, that other factors might also cause a longer-lasting Ca^{2+} release flux in frog fibers—for example, differences in the waveform of the AP in the transverse tubular system, differences in the properties of muscle charge movement, and differences in the onset of Ca^{2+} inactivation of Ca^{2+} release.

Recovery of the Fast Decay of $\Delta[Ca^{2+}]$ after a Conditioning Stimulus

The simulations indicate that the metal-free sites on both troponin and parvalbumin are largely depleted by the Ca^{2+} released with a first AP (Fig. 5, Fig. 7 C, and Fig. 11 C) and that the loss of the ability of these sites to bind Ca^{2+} is associated with a substantial reduction in the rate of decay of $\Delta[Ca^{2+}]$ evoked by a second AP initiated shortly after the first (Figs. 7 and 11). As expected from this conclusion, the simulations indicate that the reappearance of the rapid decay of $\Delta[Ca^{2+}]$ in response to an AP is strongly correlated with the recovery of the concentration of the metal-free sites on troponin and parvalbumin (Fig. 11, C and D).

Location of the Triadic Junctions Relative to the z-Line

The triadic junctions in mammalian fibers are located circumferentially around a myofibril in a narrow region that is offset ~0.5 μm from the z-line, both in slack and stretched fibers (Brown et al., 1998). This location of SR Ca^{2+} release appears to be optimized for producing an occupancy of troponin with Ca^{2+} that is as uniform as possible for a single release location and a given amount of Ca^{2+} release. The simulations of Fig. 13 confirm that this location has clear advantages when compared with the location of the triadic junctions in amphibians fibers (at the z-line). The mammalian location achieves a more uniform and generally faster occupancy of troponin with Ca^{2+} while using a smaller total concentration of released Ca^{2+}.

Calcium Movements at Short-Sarcomere Length

The furaptra Δf_{CaD} measurements of this article were performed at nonphysiological sarcomere lengths, 3.6–4.0 μm, to minimize movement artifacts in the optical records. Simulations were used to estimate the Ca^{2+} movements expected in mouse EDL fibers at a normal working sarcomere length, 2.4 μm. These simulations indicate that, with the standard SR Ca^{2+} release flux evoked by an AP, the binding of Ca^{2+} by its buffers other than troponin is more uniform at short-sarcomere length than at long-sarcomere length; in contrast, Ca^{2+} binding by troponin is less uniform at short-sarcomere length. These differences appear to arise because the average longitudinal distance over which Ca^{2+} diffuses to reach its buffers other than troponin is smaller at short-sarcomere length, while the average radial distance to reach troponin is larger.

An unanticipated observation in the simulations is that spatially averaged $\Delta[Ca^{2+}]$ is virtually identical at short- and long-sarcomere lengths (for a given Ca^{2+} release waveform); in contrast, the Δf_{CaD} response of furaptra has a somewhat larger amplitude and briefer time course at short-sarcomere length (Fig. 12). The larger and briefer Δf_{CaD} at short-sarcomere length arises because the sarcomeric gradients in $\Delta[Ca^{2+}]$ are smaller at short-sarcomere length; thus, nonlinearities in furaptra Ca^{2+} binding in and near the release compartment are smaller. Experimental observations consistent with these simulations were made previously in frog single fibers, where the amplitude of the furaptra $\Delta[Ca^{2+}]$ signal (calibrated with Eq. 3 from spatially averaged Δf_{CaD}) was found to be somewhat larger at short-sarcomere length, and its time of peak and FDHM somewhat smaller (Konishi et al., 1991).

Without information from the multicompartment simulations, it would be tempting to conclude that stretch reduces SR Ca^{2+} release (e.g., Blinks et al., 1978). Fig. 12, however, shows that stretch can reduce the measured (spatially averaged) Ca^{2+} signal without any reduction in Ca^{2+} release, thus providing a clear example of how a multicompartment model can aid in the interpretation of an experimental observation.

We thank Dr. W.K. Chandler for comments on the manuscript.

This work was supported by grants to S.M. Baylor from the National Institutes of Health (NS 17620) and a grant from the Pennsylvania Department of Health. The Department specifically disclaims responsibility for any analyses, interpretations or conclusions.

Lawrence G. Palmer served as editor.

Submitted: 18 May 2007
Accepted: 13 August 2007

REFERENCES

Baylor, S.M., and S. Hollingworth. 1998. Model of sarcomeric Ca^{2+} movements, including ATP Ca^{2+} binding and diffusion, during activation of frog skeletal muscle. *J. Gen. Physiol.* 112:297–316.

Baylor, S.M., and S. Hollingworth. 2003. Sarcoplasmic reticulum calcium release compared in slow- twitch and fast-twitch fibres of mouse muscle. *J. Physiol.* 551:125–138.

Baylor, S.M., W.K. Chandler, and M.W. Marshall. 1983. Sarcoplasmic reticulum calcium release in frog skeletal muscle fibres estimated from arsenazo III calcium transients. *J. Physiol.* 344:625–666.

Blinks, J.R., R. Rudel, and S.R. Taylor. 1978. Calcium transients in isolated amphibian skeletal muscle fibres: detection with aequorin. *J. Physiol.* 277:291–323.

Brown, I.E., D.H. Kim, and G.E. Loeb. 1998. The effect of sarcomere length on triad location in intact feline caudofemoralis muscle fibres. *J. Muscle Res. Cell Motil.* 19:473–477.

Brown, L.D., G.G. Rodney, E. Hernandez-Ochoa, C.W. Ward, and M.F. Schneider. 2007. Ca^{2+} sparks and T tubule reorganization in dedifferentiating adult mouse skeletal muscle fibers. *Am. J. Physiol. Cell Physiol.* 292:C1156–C1166.

Cannell, M.B., and D.G. Allen. 1984. Model of calcium movements during activation in the sarcomere of frog skeletal muscle. *Biophys. J.* 45:913–925.

Capote, J., P. Bolanos, R.P. Schumeier, W. Melzer, and C. Caputo. 2005. Calcium transients in developing mouse skeletal muscle fibres. *J. Physiol.* 564:451–464.

Conti, A., L. Gorza, and V. Sorrentino. 1996. Differential distribution of ryanodine receptor type 3 (RyR3) gene products in mammalian skeletal muscles. *Biochem. J.* 316:19–23.

Dirksen, R. T., and G. Avila. 2004. Distinct effects of Ca^{2+} handling caused by malignant hyperthermia and central core disease mutations in RyR1. *Biophys. J.* 87:3193–3204.

Ecob-Prince, M.S., and E. Leberer. 1989. Parvalbumin in mouse muscle in vivo and in vitro. *Differentiation.* 40:10–16.

Eisenberg, B.R. 1983. Quantitative ultrastructure of mammalian skeletal muscle. *In* Handbook of Physiology Section 10: Skeletal Muscle. L.D. Peachey, R.H. Adrian, and S.R. Geiger, editors. Williams and Wilkins, Baltimore, MD. 73–112.

Felder, E., and C. Franzini-Armstrong. 2002. Type 3 ryanodine receptors of skeletal muscle are segregated in a parajunctional position. *Proc. Natl. Acad. Sci. USA.* 99:1695–1700.

Flucher, B.E., A. Conti, H. Takeshima, and V. Sorrentino. 1999. Type 3 and type 1 ryanodine receptors are localized in triads of the same mammalian skeletal muscle fibers. *J. Cell Biol.* 146:621–629.

Gillis, J.M., D. Thomason, J. Lefevre, and R.H. Kretsinger. 1982. Parvalbumins and muscle relaxation: a computer simulation study. *J. Muscle Res. Cell Motil.* 3:377–398.

Gomez, J., P. Neco, M. DiFranco, and J.L. Vergara. 2006. Calcium release domains in mammalian skeletal muscle studied with two-photon imaging and spot detection techniques. *J. Gen. Physiol.* 127:623–637.

Gonzalez, A., W.G. Kirsch, N. Shirokova, G. Pizarro, M.D. Stern, and E. Ríos. 2000. The spark and its ember: separately gated local components of Ca^{2+} release in skeletal muscle. *J. Gen. Physiol.* 115:139–157.

Heizmann, C.W., M.W. Berchtold, and A.M. Rowlerson. 1982. Correlation of parvalbumin concentration with relaxation speed in mammalian muscles. *Proc. Natl. Acad. Sci. USA.* 79:7243–7247.

Hirota, A., W.K. Chandler, P.L. Southwick, and A.S. Waggoner. 1989. Calcium signals recorded from two new purpurate indicators inside frog cut twitch fibers. *J. Gen. Physiol.* 94:597–631.

Hollingworth, S., and M.W. Marshall. 1981. A comparative study of charge movements in rat and frog skeletal muscle fibres. *J. Physiol.* 321:583–602.

Hollingworth, S., M. Zhao, and S.M. Baylor. 1996. The amplitude and time course of the myoplasmic free $[Ca^{2+}]$ transient in fast-twitch fibers of mouse muscle. *J. Gen. Physiol.* 108:455–469.

Hollingworth, S., C. Soeller, S.M. Baylor, and M.B. Cannell. 2000. Sarcomeric Ca^{2+} gradients during activation of frog skeletal muscle fibres imaged with confocal and 2-photon microscopy. *J. Physiol.* 526:551–560.

Hollingworth, S., W.K. Chandler, and S.M. Baylor. 2006. Effects of tetracaine on calcium sparks in frog intact skeletal muscle fibers. *J. Gen. Physiol.* 127:291–307.

Jong, D.-S., P.C. Pape, S.M. Baylor, and W.K. Chandler. 1995. Calcium inactivation of calcium release in frog cut muscle fibers that contain millimolar EGTA or Fura-2. *J. Gen. Physiol.* 106:337–388.

Klein, M.G., H. Cheng, L.F. Santana, Y.-H. Jiang, W.J. Lederer, and M.F. Schneider. 1996. Two mechanisms of quantized calcium release in skeletal muscle. *Nature.* 379:455–458.

Konishi, M., and S.M. Baylor. 1991. Myoplasmic calcium transients monitored with purpurate indicator dyes injected into intact frog skeletal muscle fibers. *J. Gen. Physiol.* 97:245–270.

Konishi, M., S. Hollingworth, A.B. Harkins, and S.M. Baylor. 1991. Myoplasmic calcium transients in intact frog skeletal muscle fibers monitored with the fluorescent indicator furaptra. *J. Gen. Physiol.* 97:271–301.

Lai, F.A., Q.-Y. Liu, L. Xu, A. El-Hashem, N.R. Kramarcy, R. Sealock, and G. Meissner. 1992. Amphibian ryanodine receptor isoforms are related to those of mammalian skeletal and cardiac muscle. *Am. J. Physiol.* 263:C365–C372.

Melzer, W., E. Rios, and M.F. Schneider. 1986. The removal of myoplasmic free calcium following calcium release in frog skeletal muscle. *J. Physiol.* 372:261–292.

Murayama, T., and Y. Ogawa. 1992. Purification and characterization of two ryanodine-binding protein isoforms from sarcoplasmic reticulum of bullfrog skeletal muscle. *J. Biochem.* 112:514–522.

Novo, D., M. DiFranco, and J.L. Vergara. 2003. Comparisons between the predictions of diffusion- reaction models and localized Ca^{2+} transients in amphibian skeletal muscle fibers. *Biophys. J.* 85:1080–1097.

O'Brien, J., G. Meissner, and B.A. Block. 1993. The fastest contracting muscles of nonmammalian vertebrates express only one isoform of the ryanodine receptor. *Biophys. J.* 65:2418–2427.

Olivares, E.B., S.J. Tanksley, J.A. Airey, C.F. Beck, Y. Ouyang, T.J. Deerinck, M.H. Ellisman, and J. Sutko. 1991. Nonmammalian vertebrate skeletal muscles express two triad junctional foot protein isoforms. *Biophys. J.* 59:1153–1163.

Peinelt, C., and H.-J. Apell. 2002. Kinetics of the Ca^{2+}, H^{+}, and Mg^{2+} interaction with the ion-binding sites of the SR Ca-ATPase. *Biophys. J.* 82:170–181.

Pouvreau, S., L. Royer, J. Yi, G. Brum, G. Meissner, E. Rios, and J. Zhou. 2007. Ca^{2+} sparks operated by membrane depolarization require isoform 3 ryanodine receptor channels in skeletal muscle. *Proc. Natl. Acad. Sci. USA.* 104:5235–5240.

Raju, B., E. Murphy, L.A. Levy, R.D. Hall, and R.E. London. 1989. A fluorescent indicator for measuring cytosolic free magnesium. *Am. J. Physiol.* 256:C540–C548.

Ríos, E., and G. Pizarro. 1988. Voltage sensors and calcium channels of excitation-contraction coupling. *News in Physiol. Sci.* 3:223–227.

Robertson, S.P., J.D. Johnson, and J.D. Potter. 1981. The time-course of Ca exchange with calmodulin, troponin, parvalbumin, and myosin in response to transient increase in Ca. *Biophys. J.* 34:559–569.

Rome, L.C., D.A. Syme, S. Hollingworth, S.L. Lindstedt, and S.M. Baylor. 1996. The whistle and the rattle: the design of sound producing muscles. *Proc. Natl. Acad. Sci. USA.* 93:8095–8100.

Schneider, M.F., and B.J. Simon. 1988. Inactivation of calcium release from the sarcoplasmic reticulum in frog skeletal muscle. *J. Physiol.* 405:727–745.

Schwerzmann, K., H. Hoppeler, S.R. Kayar, and E.R. Weibel. 1989. Oxidative capacity of muscle and mitochondria: correlation of physiological, biochemical, and morphometric characteristics. *Proc. Natl. Acad. Sci. USA.* 86:1583–1587.

Sembrowich, W.L., J.J. Quintinskie, and C. Li. 1985. Calcium uptake in mitochondria from different skeletal muscle types. *J. Appl. Physiol.* 59:137–141.

Shirokova, N., and E. Ríos. 1997. Small event Ca^{2+} release: a probable precursor of Ca^{2+} sparks in frog skeletal muscle. *J. Physiol.* 502:3–11.

Smith, D.S. 1966. The organization and function of the sarcoplasmic reticulum and T system of muscle cells. *Prog. Biophys. Mol. Biol.* 16:107–142.

Woods, C.E., D. Novo, M. DiFranco, and J.L. Vergara. 2004. The action potential-evoked sarcoplasmic reticulum calcium release is impaired in *mdx* mouse muscle fibres. *J. Physiol.* 557:59–75.

Yeung, E.W., N.P. Whitehead, T.M. Suchyna, P.A. Gottlieb, F. Sachs, and D.G. Allen. 2005. Effects of stretch-activated channel blockers on $[Ca^{2+}]_i$ and muscle damage in the *mdx* mouse. *J. Physiol.* 562:367–380.

Zhao, M., S. Hollingworth, and S.M. Baylor. 1996. Properties of tri- and tetra-carboxylate Ca^{2+} indicators in frog skeletal muscle fibers. *Biophys. J.* 70:896–916.